Tectonics at the axis of the very slow-spreading Southwest Indian Ridge: Insights from TOBI sidescan sonar imagery

Olga Gomez, Anne Briais, Daniel Sauter, Véronique Mendel

Geochemistry Geophysics Geosystems G3
AN ELECTRONIC JOURNAL OF THE EARTH SCIENCES
Published by AGU and the Geochemical Society

Article
Volume 7, Number 5
3 May 2006
Q05K12, doi:10.1029/2005GC000955
ISSN: 1525-2027

Tectonics at the axis of the very slow spreading Southwest Indian Ridge: Insights from TOBI side-scan sonar imagery

Olga Gomez
LEGOS, CNRS-UMR 5566, Observatoire Midi-Pyrénées, 14 Avenue E. Belin, F-31400 Toulouse, France

Now at Department of Physics, University of Bath, Bath BA2 7AY, UK (pyxomg@bath.ac.uk)

Anne Briais
LEGOS, CNRS-UMR 5566, Observatoire Midi-Pyrénées, 14 Avenue E. Belin, F-31400 Toulouse, France

Now at Laboratoire Dynamique Terrestre et Planétaire, CNRS-UMR 5562, Observatoire Midi-Pyrénées, 14 Avenue E. Belin, F-31400 Toulouse, France

Daniel Sauter and Véronique Mendel
Institut de Physique du Globe, CNRS-ULP EMR 7516, 5 Rue René Descartes, F-67084 Strasbourg, France

[1] We present the analysis of the deformation in the axial valley of two contrasted regions of the very slow spreading Southwest Indian Ridge based on side-scan sonar images. Our objective is to investigate how the obliquity is accommodated along the system. We show that the robust magmatic segments have axial valleys and major faults subperpendicular to spreading. The other sections show fault populations with various degrees of obliquity, often arranged in left-stepping echelons, accommodating part of the strike-slip deformation. Side-scan sonar reveals the presence of a corrugated surface near 59°E interpreted to be an incipient detachment fault. We show that the large width of the SWIR oblique sections, and the difference in tectonic style between the robust volcanic segments and the magma-starved sections, is accounted for by large variations in the thickness of the brittle lithosphere. We suggest that the emplacement of mantle rocks in the surveyed amagmatic ridge sections can occur by alternating conjugate faults. Serpentinization of outcropping peridotites might also play a significant role in the development of faults in thin crust regions and the distribution of deformation in space and time.

Components: 7868 words, 17 figures, 1 table.

Keywords: mid-ocean ridges; side-scan sonar; tectonics; discontinuities.

Index Terms: 3035 Marine Geology and Geophysics: Midocean ridge processes; 3045 Marine Geology and Geophysics: Seafloor morphology, geology, and geophysics; 3040 Marine Geology and Geophysics: Plate tectonics (8150, 8155, 8157, 8158).

Received 28 February 2005; **Revised** 5 November 2005; **Accepted** 21 December 2005; **Published** 3 May 2006.

Gomez, O., A. Briais, D. Sauter, and V. Mendel (2006), Tectonics at the axis of the very slow spreading Southwest Indian Ridge: Insights from TOBI side-scan sonar imagery, *Geochem. Geophys. Geosyst.*, *7*, Q05K12, doi:10.1029/2005GC000955.

Theme: Accretionary Processes Along the Ultra-Slow Spreading Southwest Indian Ridge
Guest Editors: Catherine Mevel and Daniel Sauter

1. Introduction

[2] Accretion processes along slow-spreading mid-ocean ridges like the Mid-Atlantic ridge (MAR) are segmented by large-offset transform faults and smaller nontransform discontinuities (NTDs) [e.g., *Macdonald et al.*, 1988; *Grindlay et al.*, 1992]. The NTDs, 5 to 20 km wide, coincide with minima in crustal production along axis, and represent boundaries between spreading cells [*Kuo and Forsyth*, 1988; *Lin et al.*, 1990; *Sempéré et al.*, 1993; *Briais and Rabinowicz*, 2002; *Rabinowicz and Briais*, 2002]. Along ultra-slow spreading ridges, sections of the axis up to 100 km long are characterized by the absence of magmatic accretion [e.g., *Rommevaux-Jestin et al.*, 1997; *Sauter et al.*, 2001; *Okino et al.*, 2002; *Dick et al.*, 2003]. These authors suggest that magmatic segmentation is controlled both by the distribution of melt production in the mantle and by melt migration processes. Discontinuities also control axial geometry and accommodate the regional ridge obliquity [e.g., *Macdonald et al.*, 1988; *Sempéré et al.*, 1993].

[3] We analyze the tectonics and fault orientations along two sections of the Southwest Indian Ridge (SWIR). Our aim is to better understand how obliquity is accommodated along an ultra-slow spreading ridge away from transform faults, and the role of NTDs in accretionary processes. We interpret bathymetry and side-scan sonar data from sections of the SWIR and compare them with the slow-spreading MAR and other ultra-slow spreading ridges. Analyses of volcanic constructions and magma distribution in these SWIR sections are discussed by *Sauter et al.* [2002], *Mendel et al.* [2003], and *Sauter et al.* [2004].

2. Tectonic and Geological Setting

[4] The ultra-slow spreading SWIR separates the African and Antarctic plates at a full opening rate of 16 mm/y, with opening directions ranging from N45°E near the Bouvet Triple Junction, to N0°E close to the Rodrigues Triple Junction (RTJ) [*DeMets et al.*, 1990; *Fisher and Goodwillie*, 1997]. The rift axis is generally oblique to spreading, with variable degrees of obliquity along-ridge (Figure 1). Along-axis depth, gravity variations [*Patriat et al.*, 1997; *Cannat et al.*, 1999] and basalt chemistry [*Meyzen et al.*, 2003] suggest that the Melville Transform Fault (TF) is a major boundary in magma production and distribution. Magma production appears to be more focused, and the segmentation less stable in time, east of the Melville TF than west of it. Although regional melt supply is poor east of the Melville TF, some segments receive a very high amount of melt, as evidenced by low mantle Bouguer anomalies and shallow topography [*Rommevaux-Jestin et al.*, 1997].

[5] The SWIR segmentation is characterized by focused, magmatic segments [e.g., *Cannat et al.*, 2003], and relatively large amagmatic sections, sometimes very oblique to spreading, called nontransform discontinuities [e.g., *Mendel et al.*, 1997] or amagmatic segments [*Dick et al.*, 2003]. Such a segment (82 km long [*Sauter et al.*, 2004]) is observed east of the Melville TF, akin to those found along the Gakkel Ridge [e.g., *Kurras et al.*, 2001]. This section is characterized by the absence of volcanic constructions, positive mantle Bouguer anomalies and moderate magnetization anomalies [*Searle et al.*, 2003]. Periods of amagmatic spreading east of the Melville TF seem to be dominated by large offset, long-lived, asymmetric normal faulting [*Cannat et al.*, 2003].

3. Data Collection and Processing

[6] We use multibeam bathymetric coverage from the CAPSING [*Patriat et al.*, 1997] and FUJI [*Mével et al.*, 1998; *Tamaki et al.*, 1998] cruises. The FUJI cruise also collected high-resolution acoustic images along two axial zones of the SWIR (58°30′E–60°15′E and 63°40′E–65°40′E). The TOBI side-scan sonar [*Flewellen et al.*, 1993] operates at a frequency of 30 kHz, an average speed of 2 knots, and is towed 200 to 700 m above the seafloor. Its navigation is derived from ship navigation and cable length. Image mosaics with 6-m resolution were created using the PRISM software [*LeBas and Hühnerbach*, 1998].

[7] The sonar swath width is 6 km [*Flewellen et al.*, 1993] and mosaics used in this study were composed of two swaths in each survey area (Figures 2 and 3). Due to some overlap, the final width of the mosaic is about 10 km. This is often not enough to ensonify both walls of the very wide SWIR axial valley, which reaches 15 to 20 km, but it provides an image of the neovolcanic zone and the most recent deformation.

4. Tectonic Analysis

4.1. Interpretation of Side-Scan Sonar Imagery

[8] The intensity of sonar backscatter depends on the nature and roughness of the seafloor and the

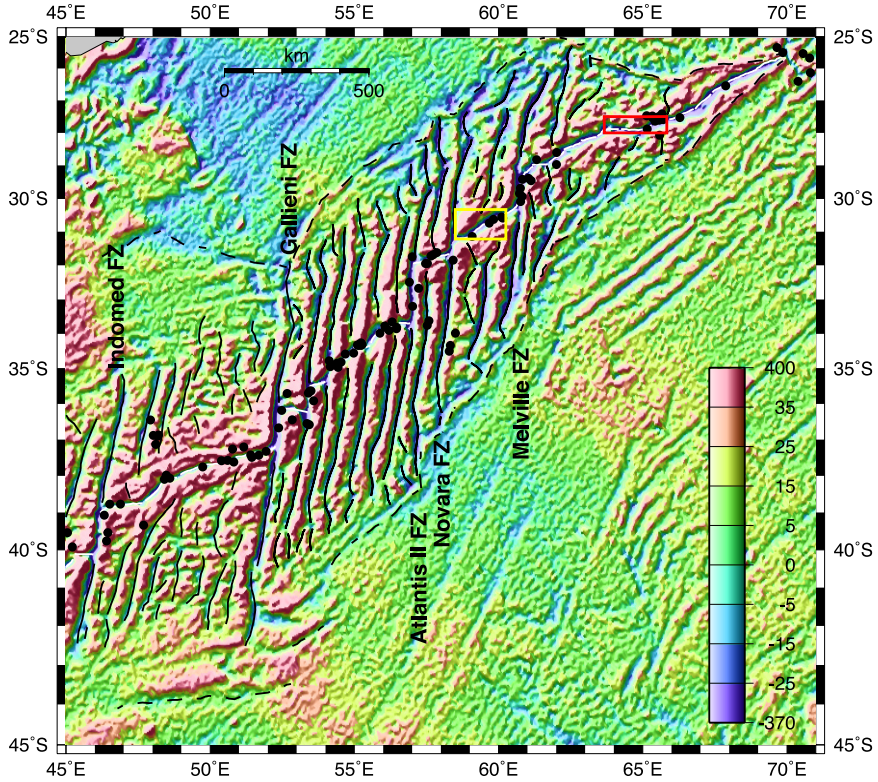

Figure 1. Shaded free-air gravity anomaly map of the SWIR [after *Sandwell and Smith*, 1997]; color scale in mGal. Solid black lines indicate fracture zones and traces of nontransform discontinuities [from *Briais and Rabinowicz*, 2002]. Black dots locate epicenters of earthquakes from the Harvard Centroid Moment Tensor database (available at http://www.seismology.harvard.edu/CMTsearch.html). The yellow and red frames mark the limits of the survey areas.

angle of incidence. Rough terrain or slopes facing the sonar show high backscatter. Bright areas in the sonar mosaics are interpreted to be recent volcanic terrains, whereas uniform, low backscatter zones likely represent sediments. We interpret bright, thin, continuous and relatively straight lines as fault scarps facing the sonar, following *McAllister and Cann* [1996]. Similar features with very low backscatter are interpreted as shadows cast by fault scarps facing away from the instrument. The narrowest of these features are fissures. The largest scarps are characterized by closely spaced, straight bathymetric contours. In this extensional context, scarps are interpreted to be normal faults [e.g., *Lawson et al.*, 1996]. Zones with relatively steep slopes in bathymetric maps, and a smooth and streaky texture in TOBI images likely represent talus of large fault scarps.

[9] Identified faults scarps and fissures were digitized. For each fracture, we calculated a mean orientation (azimuth, in positive degrees clockwise from north) and a cumulated length [*Mitchell et al.*, 2000]. Following them and *Withjack and Jamison* [1986], we used the cumulated length of fractures to characterize their populations, with normalization to an area of 1000 km^2 (Table 1). For qualitative and quantitative comparison between zones, we used rose diagrams of fracture orientations cumulated by fracture length. This methodology was used throughout the survey.

4.2. Morphology and Volcanism

[10] The FUJI cruise surveyed two contrasting axial zones of the SWIR, located on either side of the Melville TF, but where the spreading rate and NS opening direction are similar (Figures 1–3). The western study area (Figure 2 and 4–8), 58°30′E–60°15′E, is divided into three segments according to the bathymetric along-axis profile [*Mendel et al.*, 1997], numbered 15, 16 and 17 by *Cannat et al.* [1999] (respectively eastern, central and western segments of *Sauter et al.* [2002]) and two NTDs. The eastern study area (Figures 3 and 9–15), 63°40′E–65°40′E, has four segments (8, 9, 10 and 11) and three NTDs.

[11] Segments 17 (58°30′E–58°55′E), 15 (59°45′E–60°15′E, covered until 60°10′E by

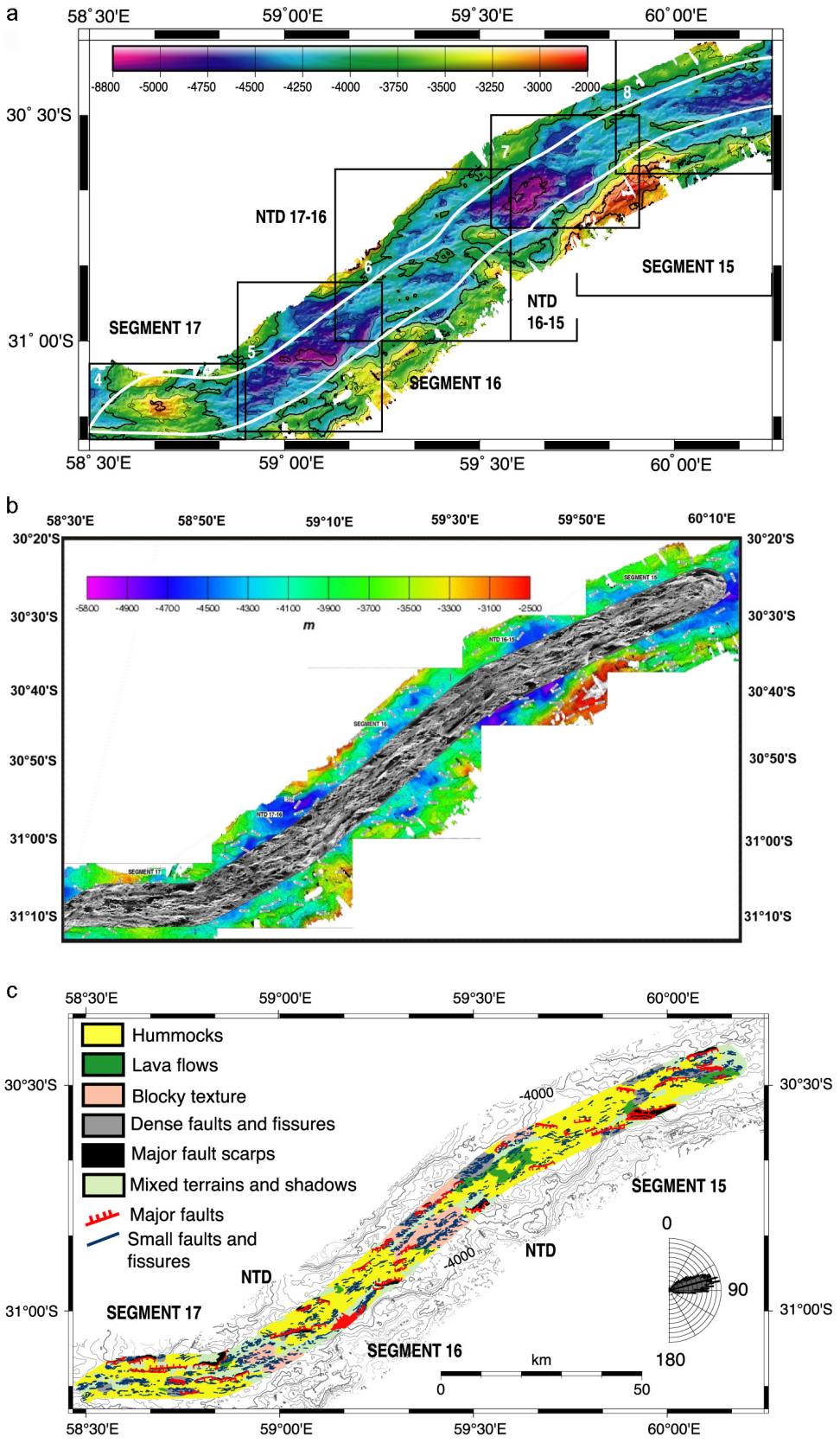
a
58°30'E
59°00'E
59°30'E
60°00'E
30° 30'S
31° 00'S
-8800 -5000 -4750 -4500 -4250 -4000 -3750 -3500 -3250 -3000 -2000
NTD 17-16
SEGMENT 17
SEGMENT 16
NTD 16-15
SEGMENT 15
b
58°30'E
58°50'E
59°10'E
59°30'E
59°50'E
60°10'E
30°20'S
30°30'S
30°40'S
30°50'S
31°00'S
31°10'S
-5800 -4900 -4700 -4500 -4300 -4100 -3900 -3700 -3500 -3300 -3100 -2500
m
c
58°30'E
59°00'E
59°30'E
60°00'E
30°30'S
31°00'S
Hummocks
Lava flows
Blocky texture
Dense faults and fissures
Major fault scarps
Mixed terrains and shadows
Major faults
Small faults and fissures
-4000
SEGMENT 15
NTD
SEGMENT 17
SEGMENT 16
0
90
180
km
0
50

Figure 2

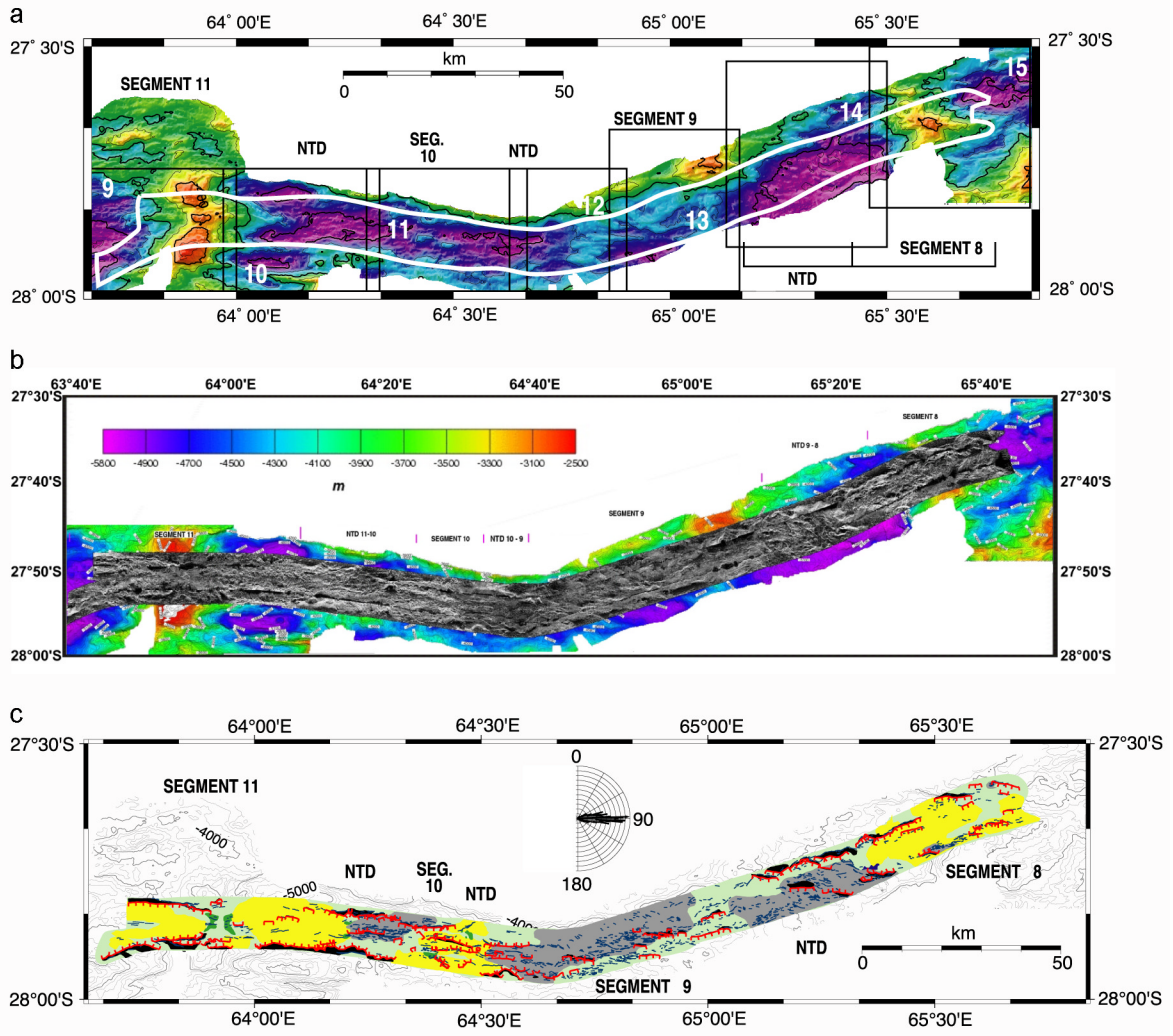

Figure 3. (a) Shaded multibeam bathymetry map of the eastern survey area between 63°20′E and 65°50′E. White solid lines show limits of side-scan sonar coverage. Black frames with white numbers locate detail Figures 9 to 15. (b) Side-scan mosaic of eastern survey. (c) Geological and structural interpretation of side-scan sonar data. Same legend as in Figure 2c. Rose diagram represents distribution of fault and fissure orientations, weighed by fracture length, binned at 1° intervals.

TOBI), 11 (63°40′E–64°10′E) and 8 (65°25′E–65°45′E) have axial valleys subperpendicular to the opening direction (Figures 4, 8–10, 15). They are robust volcanic segments centered on high bathymetric reliefs: 2000 m for segments 8 and 17, 2500 m for segment 11. Nearly their entire surface is covered with volcanic terrain. Most of it is relatively recent, but in places, lower backscatter and faults show older, more sedimented terrain.

[12] The section stretching from NTD 11-10 to NTD 10-9 (64°10′E–64°40′E) has a low obliquity (Figures 10 and 11). It is unusual because it offsets the ridge to the right, while most other SWIR discontinuities have left-stepping offsets. Both dis-

Figure 2. (a) Shaded multibeam bathymetry map of the western survey area between 58°E and 60°55′E. White solid lines show limits of side-scan sonar coverage. Black frames with white numbers locate detail Figures 4 to 8. (b) Side-scan sonar mosaic of western survey. In all sonar images, bright pixels represent high-backscatter areas. (c) Geological (see legend) and structural interpretation of side-scan sonar data. Main faults are shown in red, small fractures are shown in blue, talus is shown in gray, and fault scarps are shown in black. The detachment fault is shown in red. Rose diagram represents distribution of fault and fissure orientations, weighted by fracture length, binned at 1° intervals.

Table 1. Fracture Density and Orientations[a]

Area	Ensonified Area, km^2	Total Fault and Fissure Length, km	Normalized[b] Fault Length, km	Axial Trend, N°E	Obliquity, deg	Fault Populations N°E	Predicted Orientations, N°E
Segment 17	604	467	773	90	0	85–100	90
NTD 17-16	240	206	858	57	33		70–85 (clay)
						65–85	90 (s/s, s, a)
						90–95	65 (s/s, s)
							70–80 (s/s, a)
Segment 16	635	718	1131	53	37	60–80	70–85 (clay)
							90 (s/s, s, a)
							65 (s/s, s)
							70–80 (s/s, a)
NTD 16-15	263	141	536	64	26	40–75	70–85 (clay)
							90 (s/s, s, a)
							65 (s/s, s)
							70–80 (s/s, a)
Segment 15	582	380	653	85	5	70–80	90
Segment 11	721	97	134	90	1	85–90	90
						100–105	
NTD 11-10	342	226	225	97	6	85–95	90–100
Segment 10	222	88	396	95	4	100–110	90–100
NTD 10-9	146	54	370	95	4	105–110	90–100
Segment 9	745	374	502	72	20	80–95	80–90
NTD 9-8	395	175	443	74	18	80–85	80–90
						90–100	
Segment 8	383	127	331	90	1	70–80	90

[a] Fault and fissure orientations and comparison with predictions from analogical models of oblique rifts using clay [*Withjack and Jamison*, 1986; *Clifton et al.*, 2000] or sand and silicon [*Tron and Brun*, 1991]. Abbreviations: s/s, sand on silicon; s, symmetric spreading; a, asymmetric spreading. The direction of opening is N0°E in the western survey area and N1°E in the eastern one.
[b] Per 1000 km^2 of axial valley floor.

continuities show low backscatter, probably sedimented terrain, and are affected by landslides. In NTD 10-9, the sonar image covered the base of the northern axial valley wall. A dredge (DR15, all dredge numbers from the EDUL cruise [*Mével and the EDUL Scientific Party*, 1997]) near the base of the scarp recovered basalt, serpentine and sediments, suggesting a large vertical throw or a very thin crust. Segment 10 shows low-relief, volcanic terrain of variable relative ages.

[13] A moderately oblique section (around 20° obliquity) comprises segment 9 (64°40′E–65°11′E) and NTD 9-8 (Figures 12–14). This discontinuity forms a 30 km-large, 5600 m-deep basin (65°11′E–65°25′E). It displays high-backscatter terrain, suggesting relatively recent volcanic activity, confirmed by the glass and basalt recovered by DR12 and DR13. A circular volcano with a caldera marks the deepest part of the basin near 65°21′E, 27°44′S. East of this volcano, all the ensonified surface of the NTD is covered with hummocky lavas related with segment 8. The southwestern part of the image shows an intensively fissured, sedimented zone. Sonar images in segment 9 reveal a tectonized zone of subdued, chaotic texture where it is difficult to distinguish individual fault scarps despite an intensively fractured seafloor. No recent volcanic construction has been identified in the side-scan sonar images, or the bathymetric maps. Dredge DR14 at the base of the valley wall near 64°40′E recovered serpentine and sediments.

[14] A very oblique (53° to 64°) section of the SWIR axis comprises segment 16 and both adjacent NTDs (58°55′E–59°45′E, Figures 5–7). There, the distribution of relatively recent volcanism does not coincide with the bathymetry from which the segments were distinguished. High-backscatter, unfaulted, relatively young volcanic terrain covers the northern end of NTD 17-16, the southern part of segment 16 and most of NTD 16-15. A dredge haul near 59°25′E, 30°50′E in segment 16 (DR37) recovered basalts and sediments, confirming the interpretation of this zone as a volcanic ridge. The relatively recent volcanic terrains are continuous with those of adjacent segment 15. A "blocky" sonar texture, with low-backscatter, prism-like structures oriented

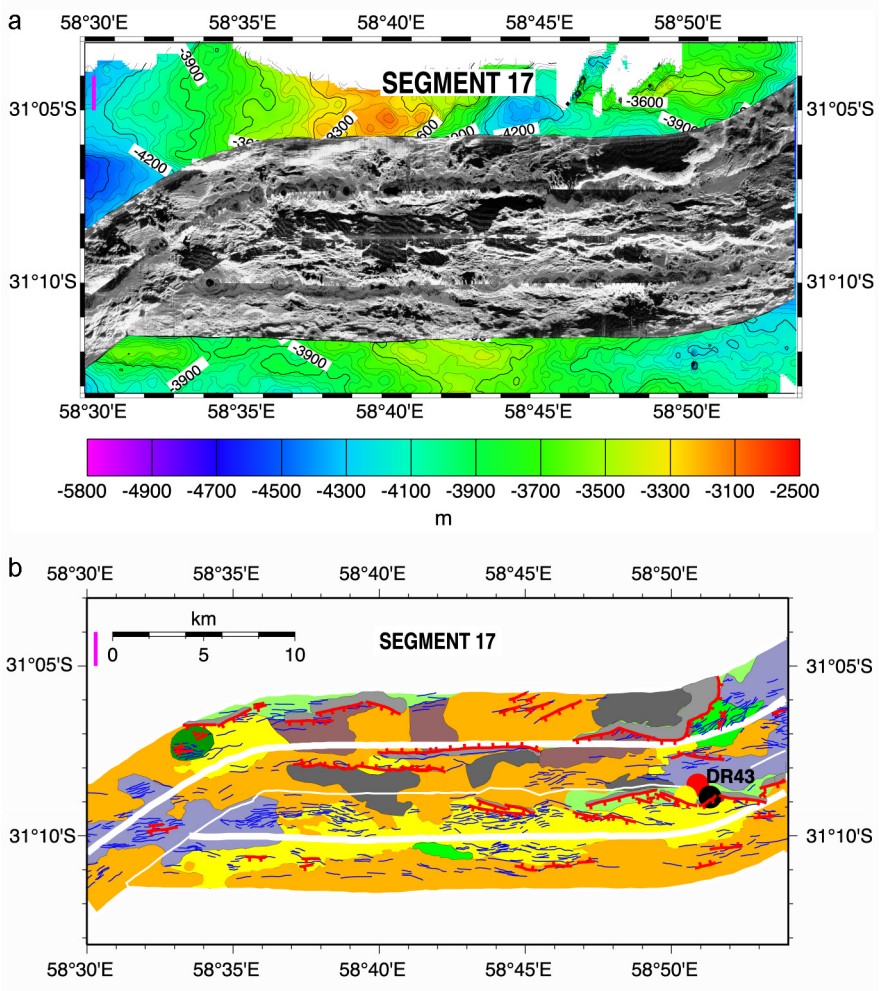

Figure 4. (a) Side-scan sonar mosaic from 58°30′E to 58°54′E, with bathymetry map outside of sonar coverage. Bright is high backscatter; dark is low backscatter. Pink ticks mark limits of segments and nontransform discontinuities (NTDs). (b) Interpretation of sonar image. Legend in Figure 5b. Red barbed lines are main fault scarps; blue lines are other fault scarps and fissures. Colored dots mark locations of dredges from EDUL cruise [*Mével and the EDUL Scientific Party*, 1997]. Color code in Figure 5b.

N80°E is observed near 58°55′E and 59°20′E. We tentatively interpret these structures as tilted blocks limited by very eroded and sedimented fault scarps. The sonar image of the northern flank of segment 16 shows a relatively smooth texture, with irregular grays, interpreted as a fault scarp partly covered with talus.

4.3. Fault Style and Distribution

[15] The deformation style and the signature of faults and fissures along the SWIR vary with the type of terrain. Fault scarps affecting relatively recent volcanic constructions appear sharper in the sonar images than fault scarps in less volcanic areas. In the sonar images of SWIR sections where no recent volcanic activity is recognized, faults are difficult to identify (Figures 11 to 14). The extent of such areas is much larger than observed on faster spreading ridges like the MAR [*Briais et al.*, 2000]. One cause for this contrast is the submarine erosion process of the fault scarps, controlled by fault activity, gravity and rock weathering [*Allerton et al.*, 1995; *Mitchell et al.*, 2000].

[16] The number of faults and fissures is generally higher in the western survey area (Table 1). Segment 11 has an especially low density of faults and fissures (Table 1). This contrast between the fault density in the two zones might be partly explained by the intensive volcanic activity in segments 11 and 8 (Figures 9 and 15) where volcanic constructs are relatively un-faulted. Another explanation is the absence of clear fault scarps in segment 9.

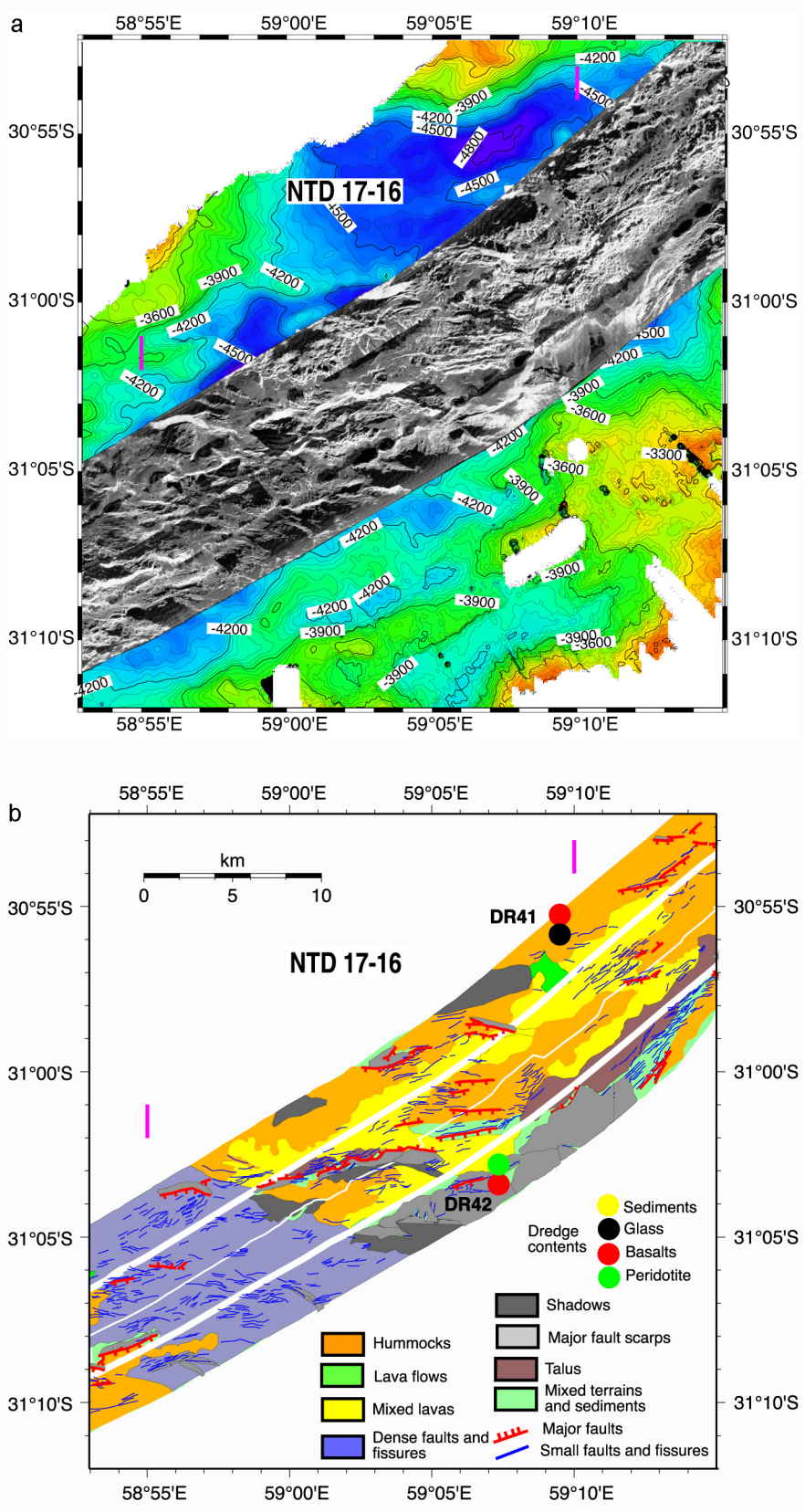

Figure 5. (a) Side-scan sonar mosaic from 58°53′E to 59°15′E. (b) Structural interpretation of Figure 5a. Legend in frame and as in Figure 4b. Note corrugated surface near 59°10′E, 31°02′E.

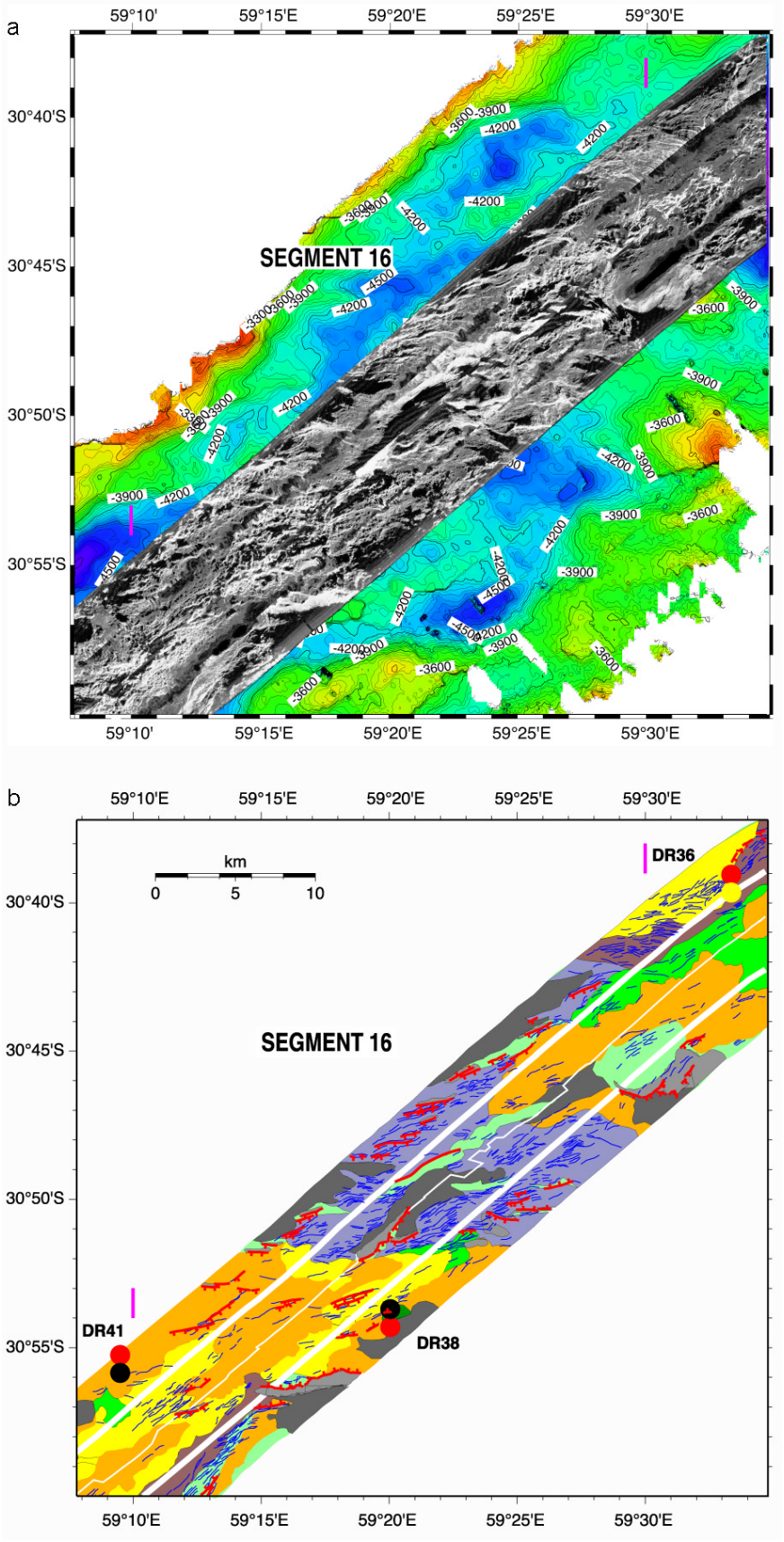
a
59°10'
59°15'E
59°20'E
59°25'E
59°30'E
30°40'S
30°45'S
30°50'S
30°55'S
SEGMENT 16
b
km
0
5
10
DR36
DR41
DR38

Figure 6

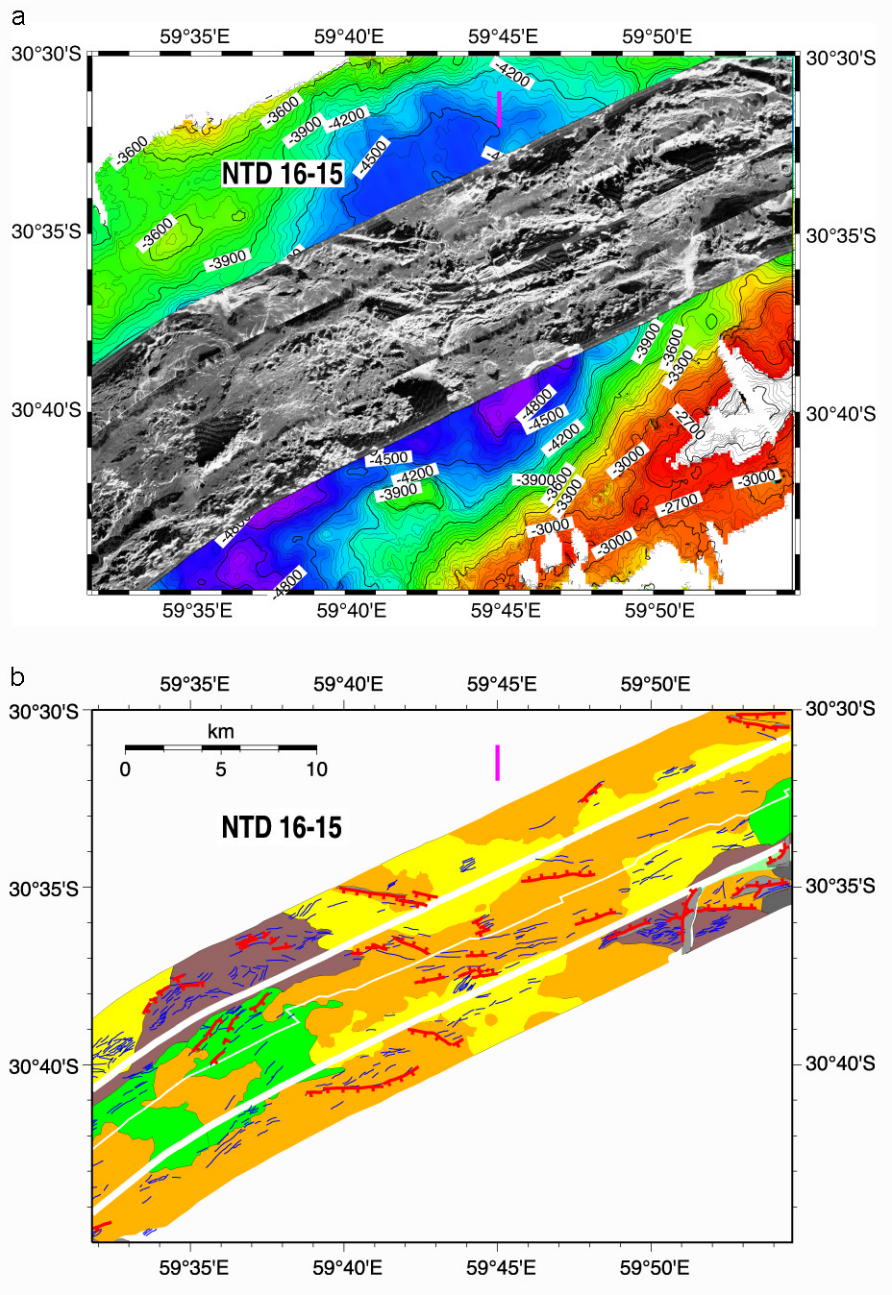

Figure 7. (a) Side-scan sonar mosaic from 59°32′E to 59°54′E. (b) Structural interpretation of Figure 7a. Same legend as in Figures 4b and 5b.

[17] Most large fault scarps observed in the sonar images coincide with the inner valley walls, or with horst-and-graben tectonics affecting axial volcanic ridges. Their vertical throws range between 400 and 1000 m, and their length reaches tens of kilometers. In segments 11, 15 and 17, synthetic normal faults form graben about 5 km wide. A relatively narrow axial valley, about 10 km wide, also characterizes these zones. At segment 17, an E-W trending fault scarp joins a N40°E-trending one, both facing south to southeast and with large throws (200 to 300 m). Similar fault patterns are frequently observed in the MAR, where they limit intersection highs [e.g., *Escartín et al.*, 1999].

Figure 6. (a) Side-scan sonar mosaic from 59°08′E to 59°35′E. (b) Structural interpretation of Figure 6a. Same legend as in Figures 4b and 5b.

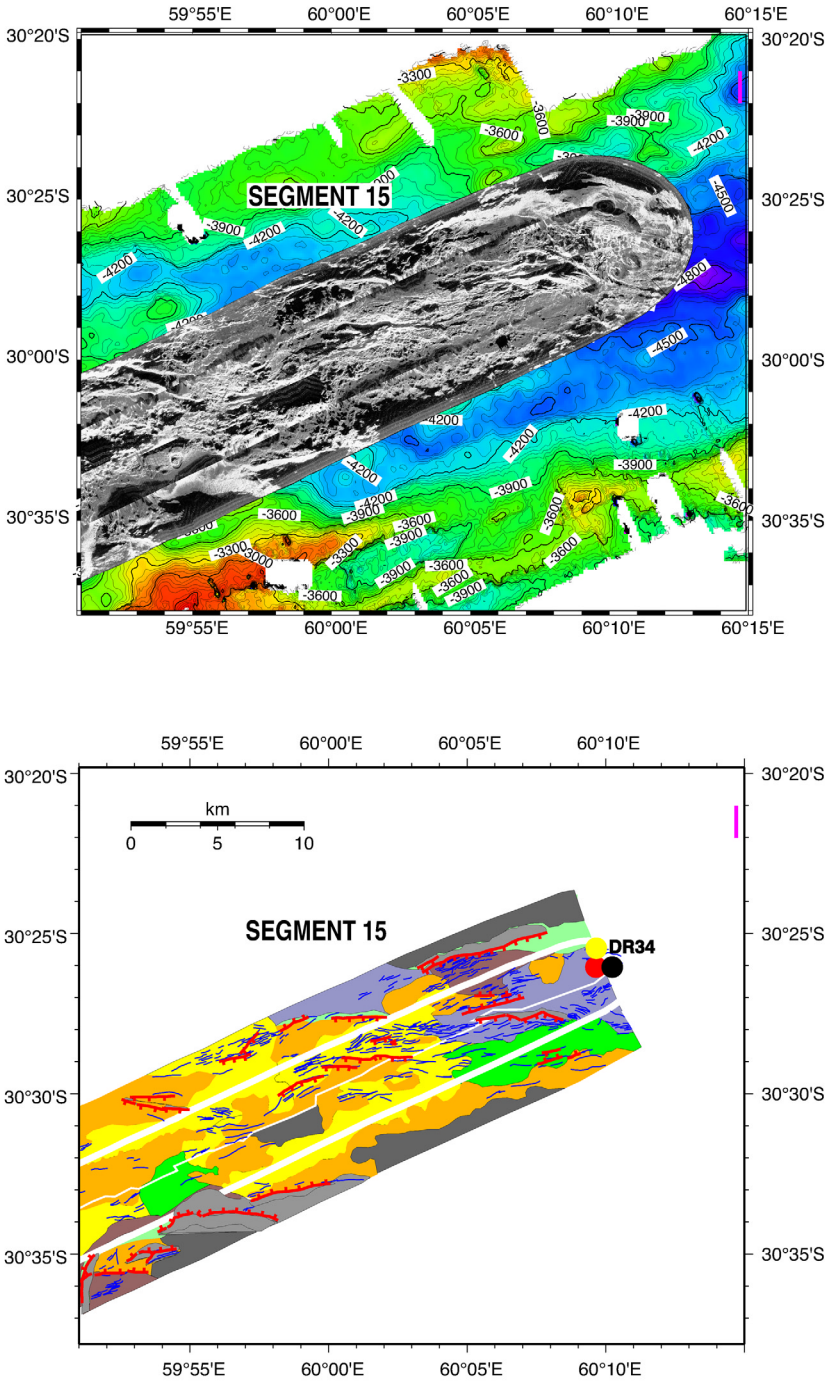

Figure 8. (a) Side-scan sonar mosaic from 59°51′E to 60°15′E. (b) Structural interpretation of Figure 8a. Same legend as in Figures 4b and 5b.

Zones of closely spaced faults and fissures, often a few tens of meters apart, are observed mostly near the axial valley walls, in-between volcanic ridges, and as relays between fault segments.

[18] Shorter fault scarps, often arranged en echelon, are found in discontinuities or in oblique segments. Examples of these are observed in segment 16, near 59°20′E, 30°45′S (Figure 6), or in segment 15 near 60°E, 30°30s (Figure 8). They reflect the accommodation of shear in these areas [*Briais et al.*, 2000]. Other fault patterns also suggest strike-slip displacement. Near

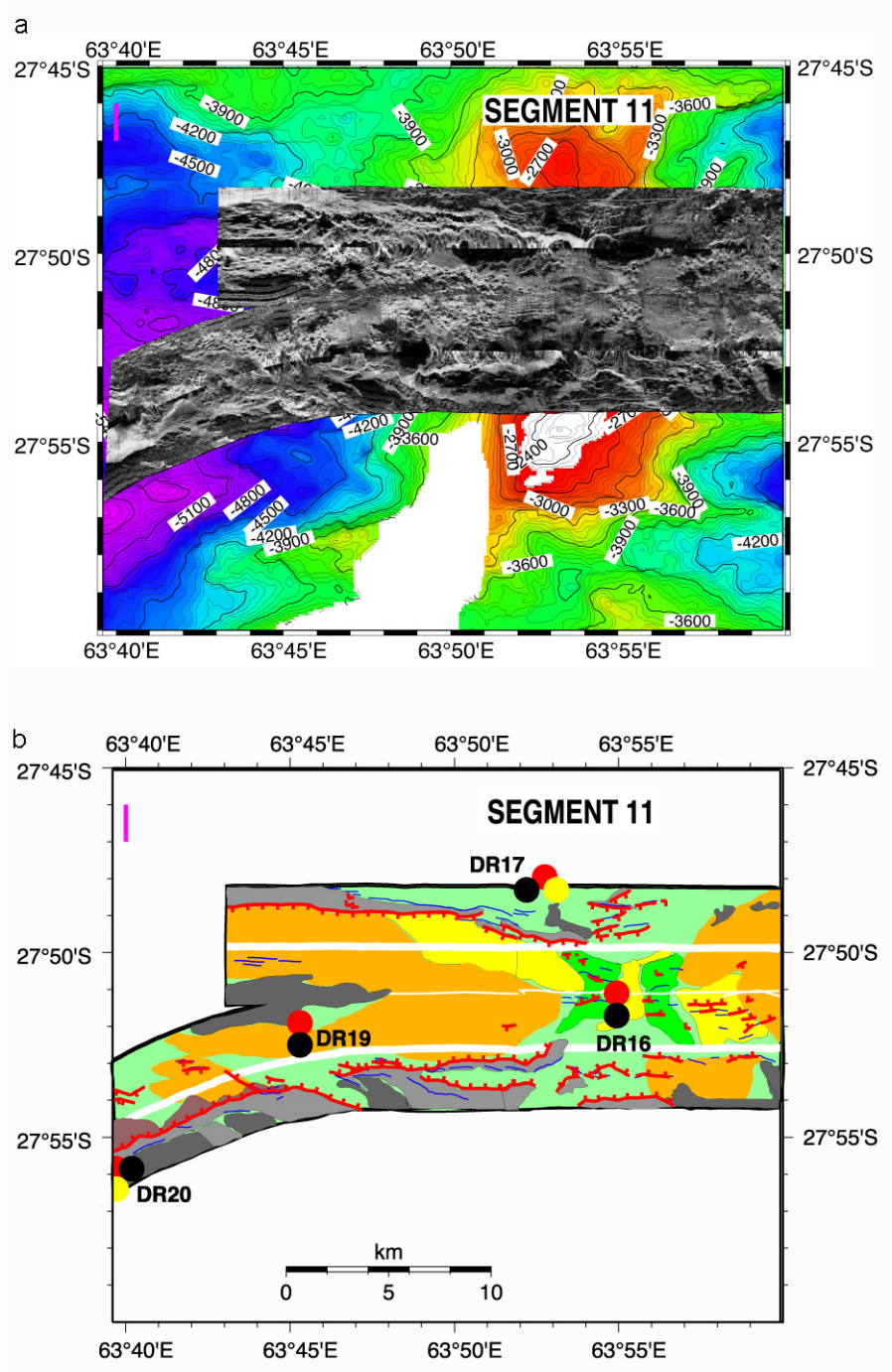

Figure 9. (a) Side-scan sonar mosaic from 63°40′E to 64°00′E. (b) Structural interpretation of Figure 9a. Same legend as in Figures 4b and 5b.

59°54′E in the NTD16-15, a N05°E-trending scarp appears to be connecting to E-W-trending, smaller fault scarps forming a fault splay. Such an arrangement is interpreted to result from a strike-slip component on the main fault scarp [e.g., *Manighetti*, 1993]. It suggests that the main, highly oblique fault accommodates right-lateral strike-slip motion [*Sylvester*, 1988].

[19] In NTD 17-16 we observe a large, northward facing fault scarp with north-south corrugations (59°10′E, 31°01′S) bounding a 500-m high, gently sloping promontory. By analogy

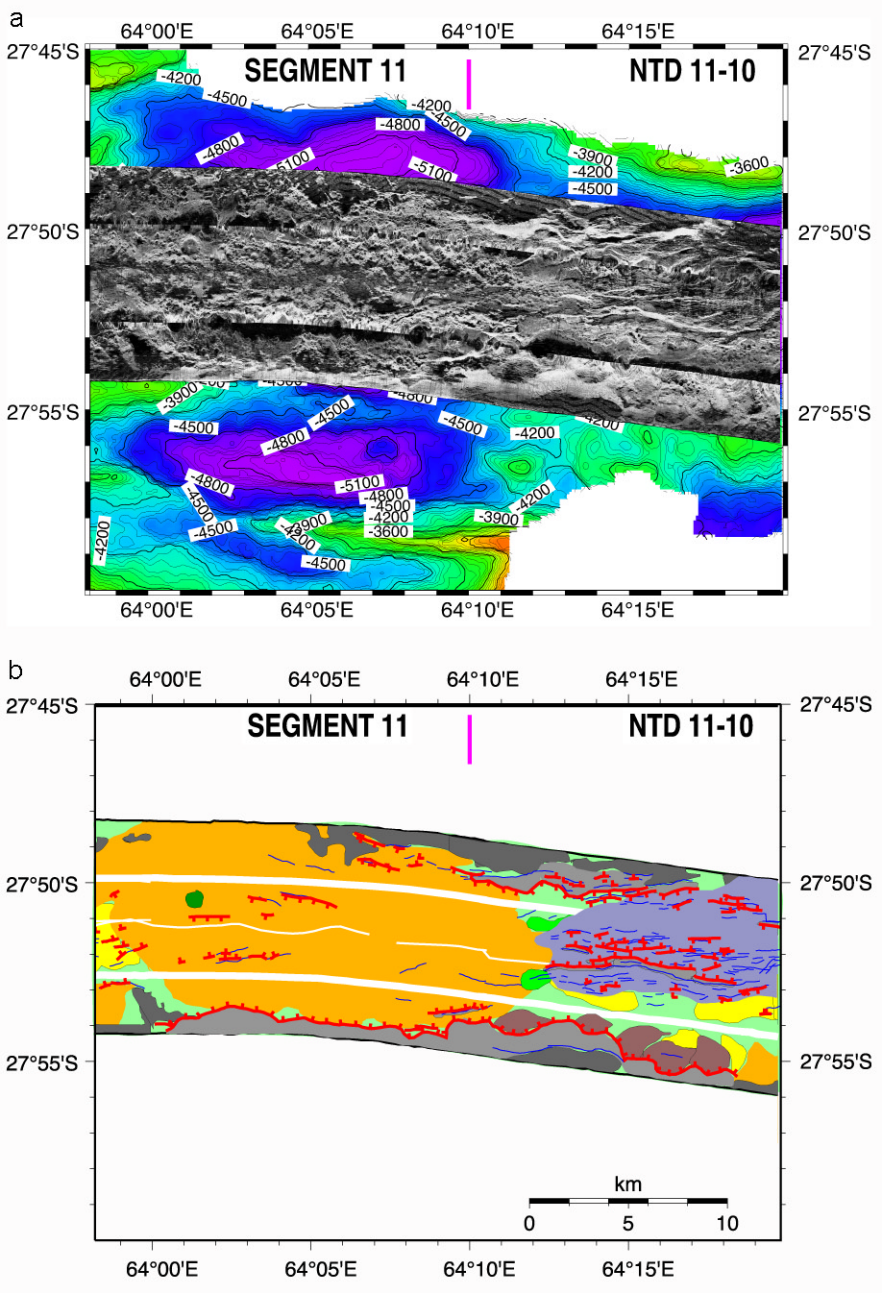

Figure 10. (a) Side-scan sonar mosaic from 63°58′E to 64°20′E. (b) Structural interpretation of Figure 10a. Same legend as in Figures 4b and 5b.

with corrugated fault scarps described in the Atlantic as megamullions, or subhorizontal faults [e.g., *Cann et al.*, 1997; *Tucholke et al.*, 1997, 1998; *Canales et al.*, 2004], we interpret this scarp to be an incipient detachment fault. At 59°07′E, 31°03′S, DR42 recovered basalt and serpentine, suggesting the local outcropping of mantle rocks. A much larger detachment fault (FUJI Dome) was identified off-axis near 64°E, south of segment 11, from side-scan sonar images and submersible dives (Shinkai 6500 dives 444, 445 and 450 [*Fujimoto et al.*, 1999]), revealing a 1 My-long accumulation of motion along a normal fault [*Searle et al.*, 2003]. Several other detachment faults have since been discovered on the flanks of the eastern SWIR [*Cannat et al.*, 2004]. Within the axial survey area, we have not observed other faults that could imply large asymmetry in the axial valley deformation.

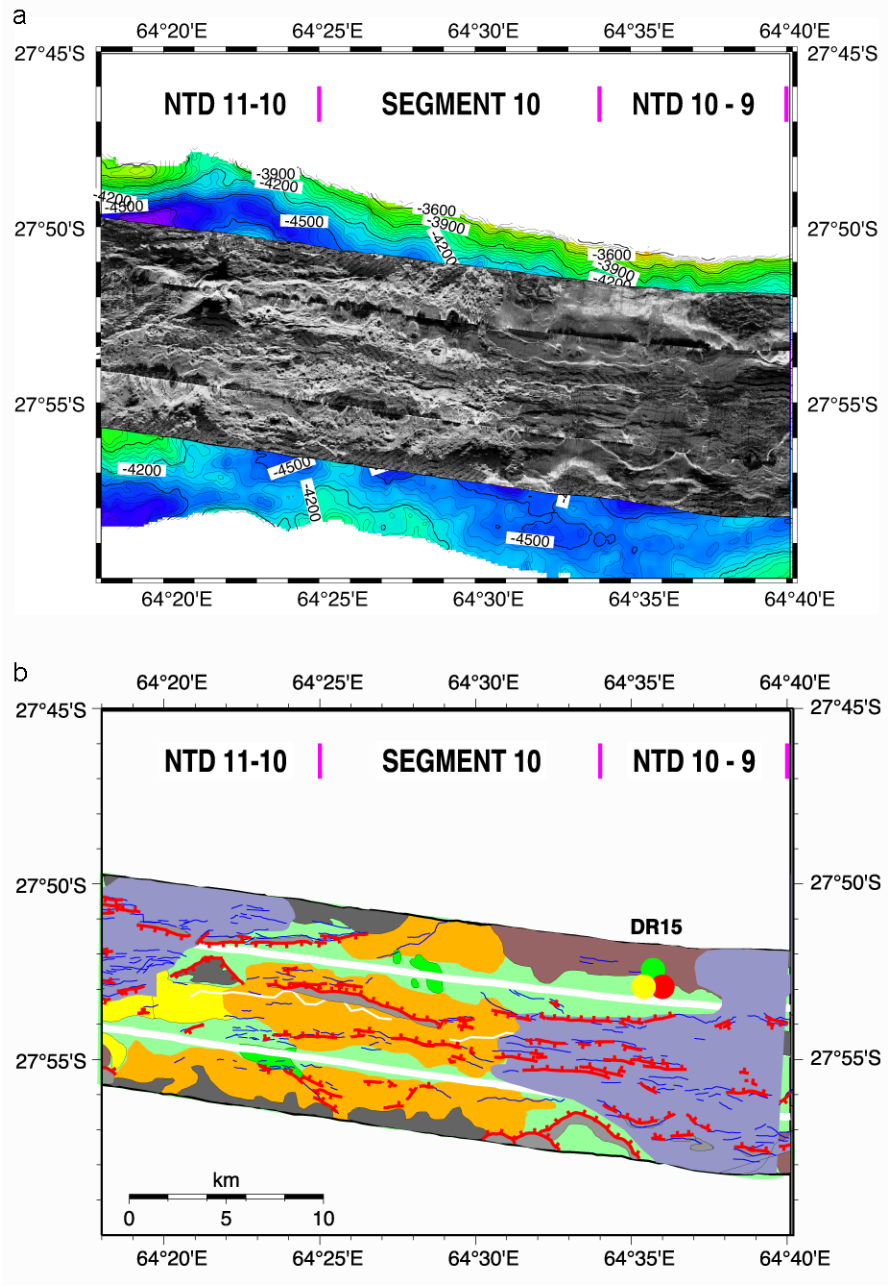

Figure 11. (a) Side-scan sonar mosaic from 64°18′E to 64°40′E. (b) Structural interpretation of Figure 11a. Same legend as in Figures 4b and 5b.

4.4. Fracture Orientation and Oblique Spreading

[20] The main volcanic segments (segments 8, 11, 15 and 17) show large fault scarps oriented E-W to N80°E, subperpendicular to the N-S opening direction. Large scarps forming the inner valley walls rarely have oblique orientations, as observed in segments 15 and 8 (Figures 8, 14–16). Some faults near discontinuities have azimuths close to N75°E (segments 17 and 15) and to N60°E (segment 8). These oblique faults could reflect a rotation of the extensional stresses approaching the discontinuity, as happens in the MAR and other sections of the SWIR [*Grindlay et al.*, 1992; *Grindlay and Fox*, 1993; *Parson et al.*, 1997].

[21] All other surveyed sections have obliquities from a few to almost 40°. Fault orientations measured in the two SWIR sections generally agree with predictions of clay models [*Withjack and Jamison*, 1986; *Clifton et al.*, 2000] and sand/silicon models [*Tron and Brun*, 1991] for oblique

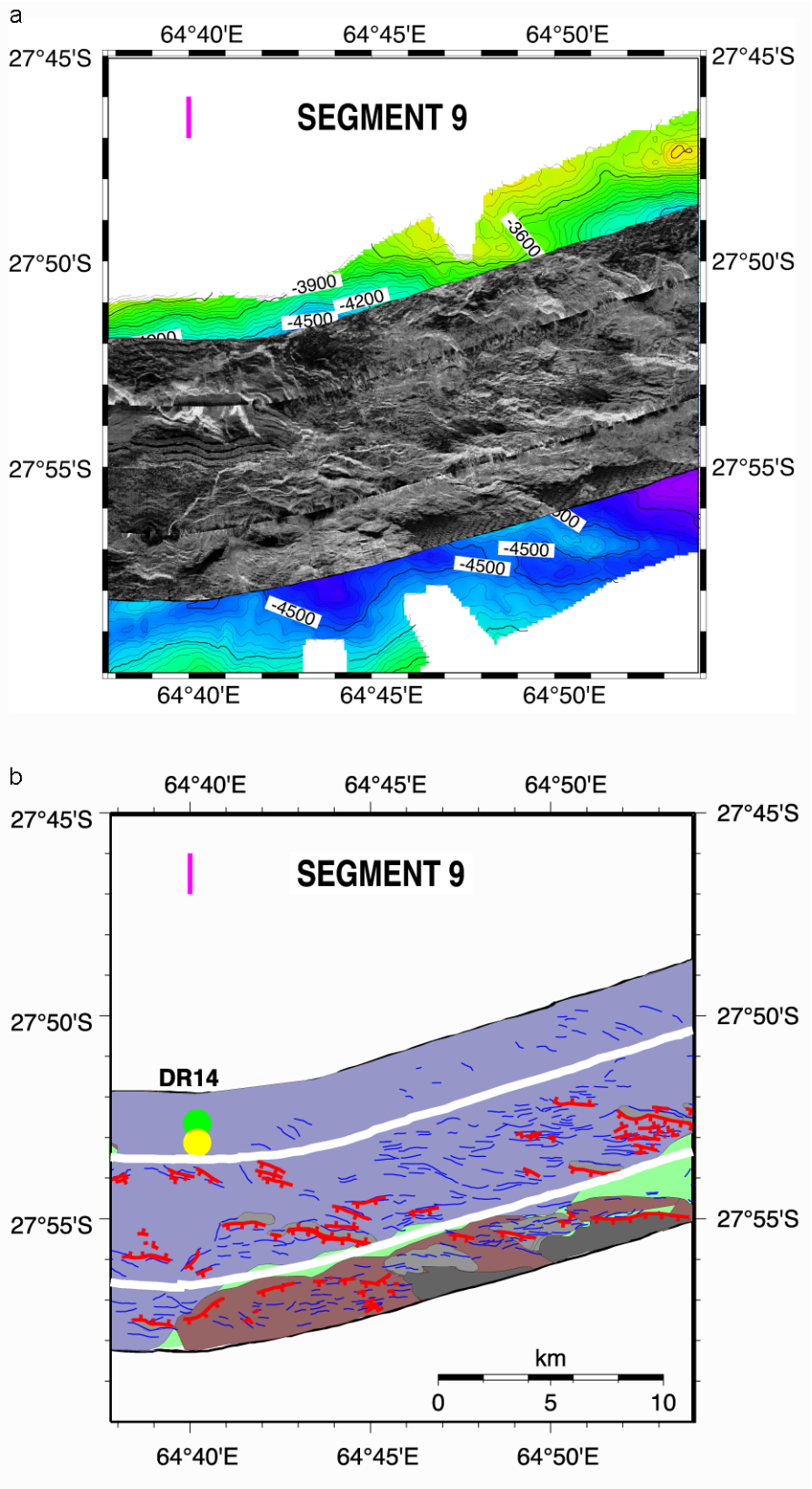

Figure 12. (a) Side-scan sonar mosaic from 64°38′E to 64°54′E. (b) Structural interpretation of Figure 12a. Same legend as in Figures 4b and 5b.

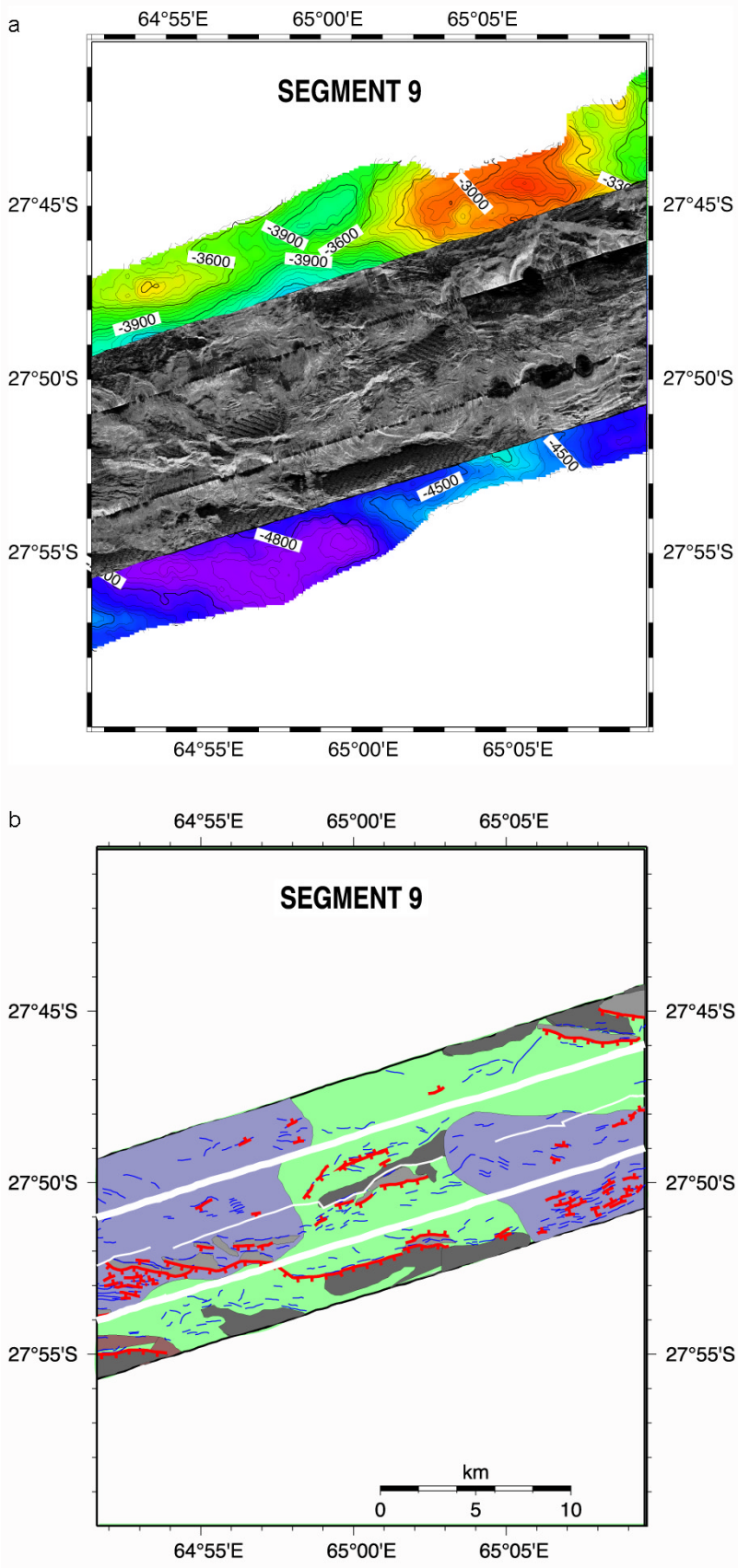
a
64°55'E
65°00'E
65°05'E
SEGMENT 9
27°45'S
27°50'S
27°55'S
-3000
-3900
-3600
-4500
-4800
b
km
0
5
10

Figure 13

rifts. Experiments show that normal faults are oriented obliquely both to the direction of spreading and to the direction of the rift (Table 1). Fault orientations depend mostly on the obliquity angle α, defined as the angle between the rift direction and the opening direction. Within our study area, α varies between 53° and 90°.

[22] Segment 9 and NTD 9-8 have an obliquity α close to 72° (Table 1). We observe N90°E-trending faults in segment 9, and three fault populations in the NTD 9-8, oriented N80°E, N95°E and N120°E (Figure 16b). The clay models predict the development of normal faults, with azimuths of N80°E to N90°E [*Withjack and Jamison*, 1986; *Clifton et al.*, 2000], which explains most observations but not all.

[23] The section from NTD 11-10 to NTD 10-9 has an axial valley oriented N100°E, with α of about 80° but an inverse obliquity (right-stepping offset). Faults orientations are close to N95°E (Figure 16). Main scarps associated with axial valley walls and most of the fractures are oriented N95°E to N110°E. These orientations are well explained by the three models [*Withjack and Jamison*, 1986; *Tron and Brun*, 1991; *Clifton et al.*, 2000].

[24] NTDs 16-15 and 17-16, and segment 16 have an axial valley oriented 55–65°. They show two fault populations, one subperpendicular to the opening, the other close to N70°E–N85°E. Analogical models predict the formation of faults with a large variety of orientations. Clay models predict the development of faults trending N70-85°E [*Withjack and Jamison*, 1986; *Clifton et al.*, 2000]. The model by *Tron and Brun* [1991], which includes brittle and ductile material, predicts the development of two populations, one close to N90°E and the other trending N65°E to N80°E (Table 1). These results explain the various fault populations we observe.

[25] Other natural ridge systems are oblique to spreading, with α varying between 40 and 60°: the Gulf of Aden ridge [*Audin*, 1999; *Dauteuil et al.*, 2001], the Reykjanes ridge [*Murton and Parson*, 1993; *Parson et al.*, 1993] and Mohn's ridge [*Dauteuil et al.*, 1990; *Dauteuil and Brun*, 1996]. These latter two systems show two main fault populations, one subperpendicular to the opening direction, comparable to the results obtained for the SWIR, and another parallel to the axis, rarely observed in the SWIR. In the Gulf of Aden, *Dauteuil et al.* [2001] describe two populations of faults for a moderate obliquity: one accommodating the extensional deformation only and the other made of en echelon faults with strike-slip components 10 to 20° oblique to the perpendicular to the opening direction. We observe similar patterns along the SWIR.

[26] Comparison of our results with laboratory experiments and with other natural systems show that most fault trends observed along the SWIR are explained by ridge obliquity. Yet the orientations that remain unexplained with the models, and the discrepancies between natural systems suggest that other factors may influence the direction of stress and strain in the oblique rifts. These could include mantle temperature variations, distinct upwelling geometries or variations in lithospheric strength, as is the case for the Reykjanes Ridge [*Tuckwell et al.*, 1998].

[27] The unusual N100°E orientation of the axial valley in the zone 64°10′E–64°40′E might result from an effect of the thermal structure around segment 11. This segment is particularly well fed, and might be associated with mantle upwelling. This could have thermal and mechanical effects on the overlying lithosphere and cause a rotation of local stresses. The peculiar geometry of this section might also result from the kinematic evolution of the RTJ, since the traces of the triple junction also change orientation in this section. The reverse offset may be a heritage of the primitive geometry of the ridge, when it was created at the RTJ 20 to 10 my ago [*Patriat et al.*, 1997]. A similar orientation of the RTJ trace is also observed near 68°30′E, and the present-day axial segment is less oblique than its neighbors [*Mendel et al.*, 2000].

5. Discussion

5.1. Width of SWIR Discontinuities and Rheology of the Axial Lithosphere

[28] A major observation in both studied areas is the extensive length of regions that are oblique to the opening direction (usual direction of transform faults) and to its perpendicular (usual direction of segments), relative to the moderate length of spreading-perpendicular segments. The western area accommodates more ridge offset than the

Figure 13. (a) Side-scan sonar mosaic from 64°51′E to 65°09′E. (b) Structural interpretation of Figure 13a. Same legend as in Figures 4b and 5b.

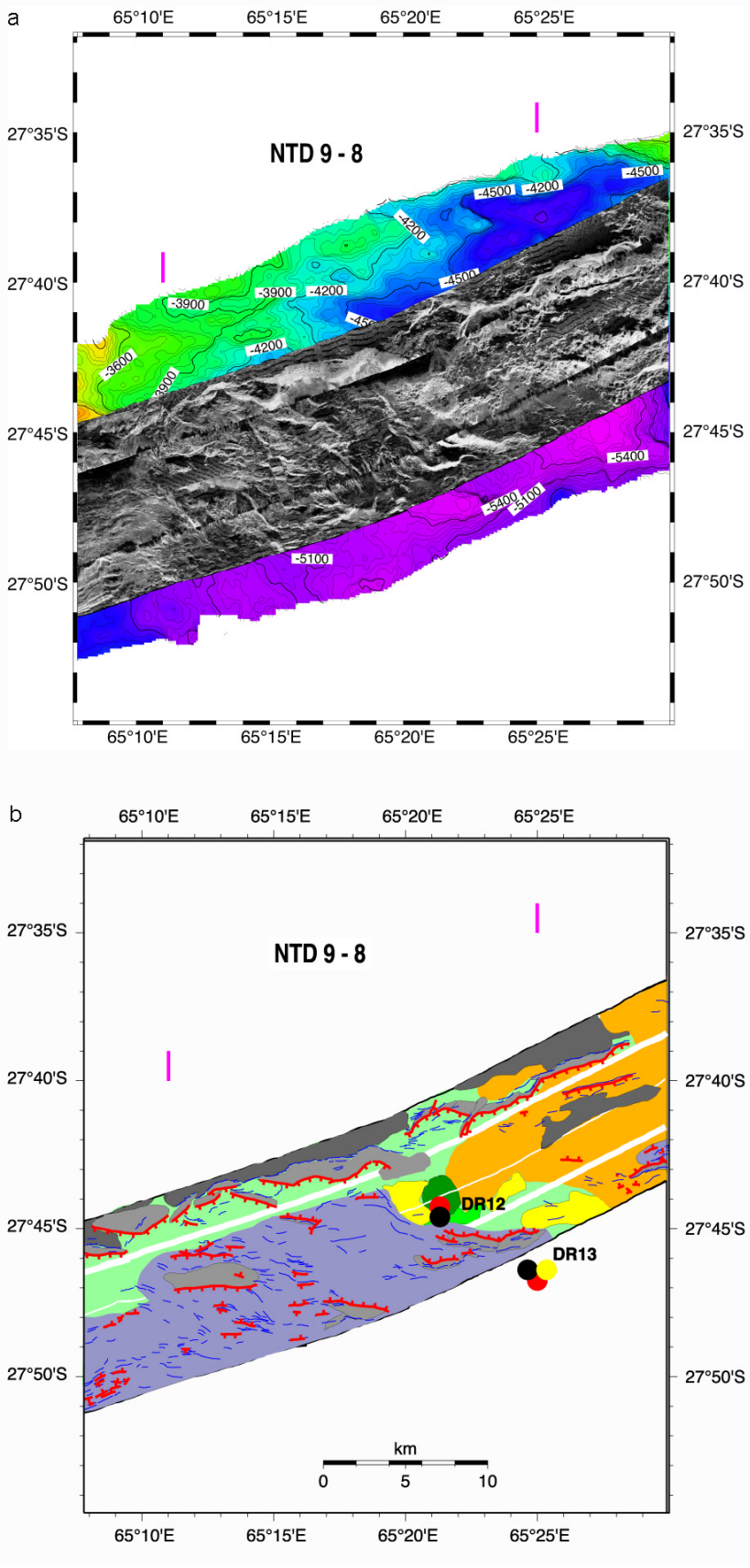
a
65°10'E
65°15'E
65°20'E
65°25'E
27°35'S
27°40'S
27°45'S
27°50'S
NTD 9 - 8
-4500
-4200
-3900
-3600
-5400
-5100
b
NTD 9 - 8
DR12
DR13
km
0
5
10

Figure 14

eastern area, with variable local obliquity. The axial valley is perpendicular to spreading in segments 17, 15, 11 and 8 only (Table 1), that is where magmatic activity is significant and the crust is thicker [*Rommevaux-Jestin et al.*, 1997]. The obliquity of the SWIR and the cumulative offset are therefore accommodated in the other sections, which received less magma recently. Such amagmatic, oblique sections in both FUJI boxes are about 80 km long, compared to about 20 km on the MAR [*Briais et al.*, 2000; *Parson et al.*, 2000]. In other parts of the SWIR or the Gakkel ridge, they reach 180 km in length [*Dick et al.*, 2003].

[29] These variations in ridge obliquity are not only correlated to magma supply, but also to variations of the width of the axial valley. Bathymetry data show variations of the axial valley width from 10 km in magmatically robust segments to more that 20 km for oblique, amagmatic sections.

[30] We suggest that these observations imply large variations in the SWIR brittle lithosphere thickness (Figure 17), as inferred from the results of analogical models [*Allemand and Brun*, 1991; *Mauduit and Dauteuil*, 1996]. Considering that the width (W) of a rift is proportional to the thickness of the elastic lithosphere (T) and the dip of the bounding faults (D) according to the equation: $\tan D = 2*T/W$ [*Allemand and Brun*, 1991], and assuming a fault dip of 60 ± 10° for faults in the oceanic crust [*Mauduit and Dauteuil*, 1996], the thickness of the brittle lithosphere under a 10 km-wide axial valley is estimated to be between 6 and 14 km (9 km for 60°-dipping faults), and between 14 and 27 km (17 km for 60° dip) under a 20 km-wide valley. Variations in the SWIR axial valley width therefore imply variations in brittle layer thickness by a factor of two between magmatically robust segments and amagmatic sections. *Mauduit and Dauteuil* [1996] model of axis discontinuity has a brittle, elastic layer of variable thickness, and a ductile layer, with an imposed offset in the rift system. Their results show that the width of the discontinuity increases with the thickness of the elastic layer. In their study, the difference in elastic layer thickness represents the contrast between a slow-spreading ridge (thick) and a fast spreading ridge (thin [*Mauduit and Dauteuil*, 1996]). We suggest that these results may be extrapolated to very slow or ultra-slow spreading ridges, where the thickness of the brittle layer thus also changes along-axis with the thermal state of the ridge, related to magma supply. In magmatically starved zones like segments 16 or 9, and adjacent discontinuities, the brittle-ductile boundary is likely to be deep, explaining the great length of oblique sections (Figure 17).

5.2. Roles of Brittle Layer Thickness and Serpentinization in the SWIR Tectonic Style

[31] One puzzling observation in our survey areas is the very small number of large normal faults that could represent evidence for asymmetric accretion. Our observations show large fault scarps, often forming symmetrical graben in ridge-perpendicular sections, and multiple, en échelon, short faults in the oblique, less magmatic sections (Figures 2 and 3). We only observe one large corrugated fault scarp near 59°10′E in the side-scan sonar data, which is a good candidate for a low-angle normal fault. Part, but not all of this absence may be due to the lack of coverage of the axial valley edges by sonar data.

[32] Two factors could control the SWIR fault distribution and deformation style. First, the large thickness of the brittle lithosphere under some amagmatic SWIR sections could prevent the development of large detachment faults. Using numerical modeling, *Lavier and Buck* [2002] show that when the brittle thickness of the lithosphere is very high, a rift develops by multiple conjugate faults evolving in a set of grabens rather than by asymmetric faulting creating a half-graben. We suggest that the extensional processes and the emplacement of mantle rocks in the axial valley may thus occur by alternating conjugate faults, as described for the 15°20′N MAR section [*Lagabrielle et al.*, 1998].

[33] Alternatively, the deformation on long amagmatic sections of the eastern box could also be controlled by peridotite serpentinization. It is clear from sampling and submersible dives that mantle rock outcrops form a significant part of the seafloor. It is also inferred from gravity analysis that the crustal thickness becomes very low at the SWIR amagmatic sections [*Rommevaux-Jestin et al.*, 1997]. *Escartín et al.* [1997] show that at segment scale, sections with peridotite tend to have a better localization of the deformation than more

Figure 14. (a) Side-scan sonar mosaic from 65°08′E to 65°30′E. (b) Structural interpretation of Figure 14a. Same legend as in Figures 4b and 5b.

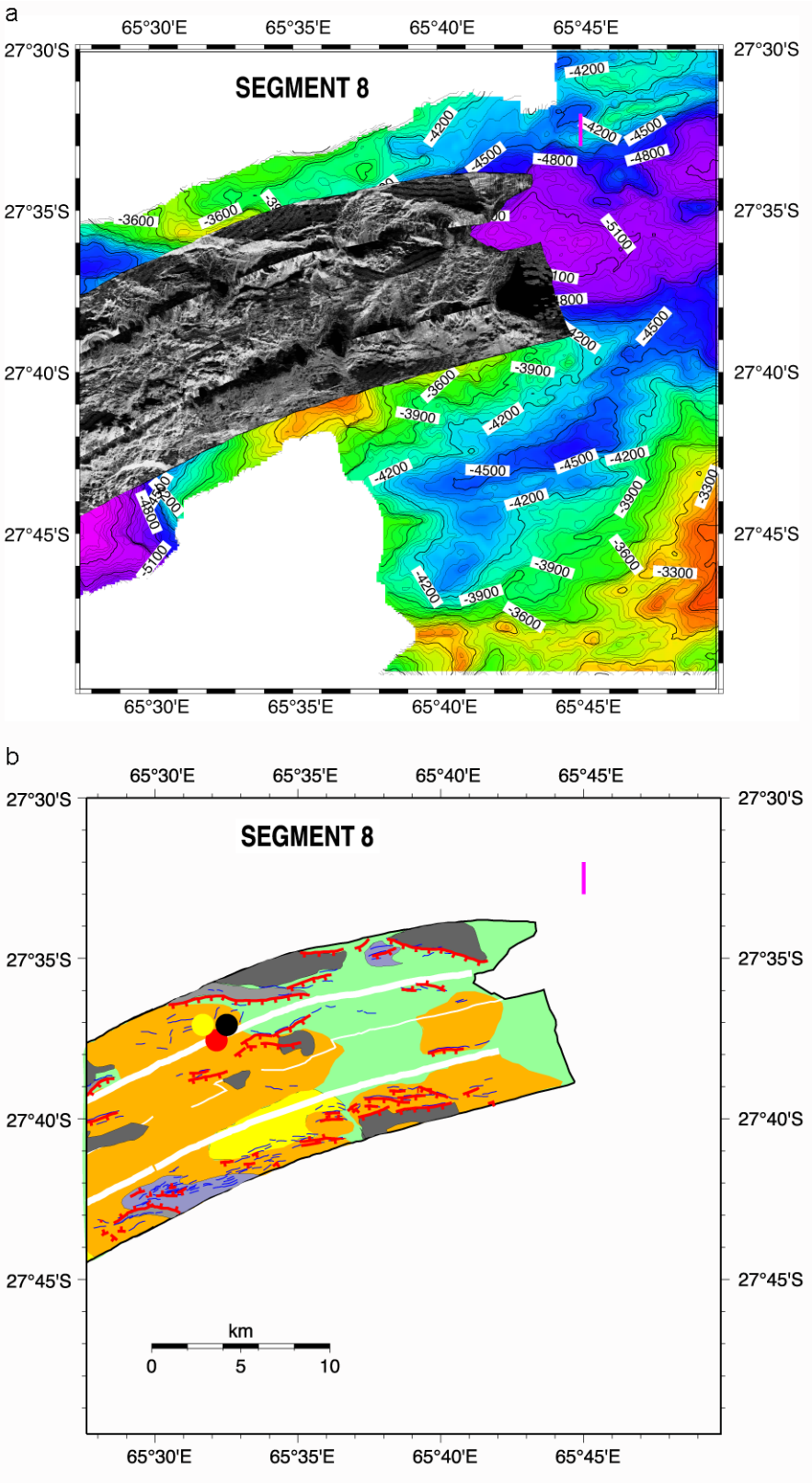

Figure 15. (a) Side-scan sonar mosaic from 65°28′E to 65°50′E. (b) Structural interpretation of Figure 15a. Same legend as in Figures 4b and 5b.

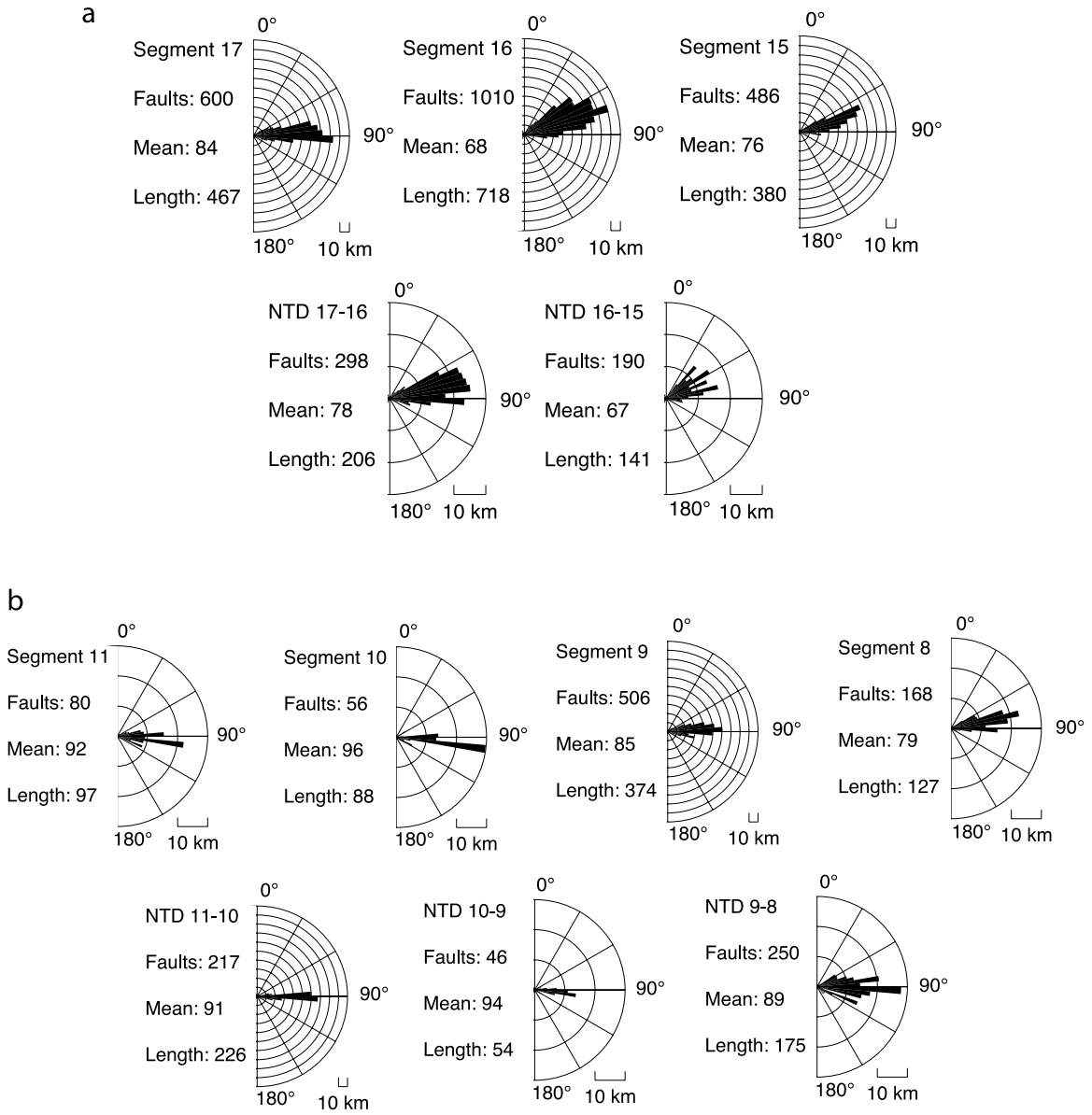

Figure 16. (a) Distribution of fault and fissure orientations in the western survey area, binned at 5° intervals. Distributions have been computed with each value weighted by the fault length following *Mitchell et al.* [2000]. Also indicated for each diagram are fracture number, mean orientation in degrees from north, and total fracture length in kilometers. (b) Distribution of fault and fissure orientations in eastern survey area. Same legend as in Figure 16a.

magmatic sections with thicker crust. The large amagmatic zone encountered in FUJI eastern box consists of terrain with smooth topography and streaky sonar textures. A similar texture observed in the MAR corresponds to talus in a discontinuity zone [*Briais et al.*, 2000], where dredges recovered sediments with some serpentine blocks [*Cann et al.*, 1997]. Most peridotites sampled in the surveyed SWIR area are 60 to 90% serpentinized [*Seyler et al.*, 2003]. The development of talus along such scarps is probably favored by the easy weathering of mantle peridotites, resulting in large, streaky sonar textures. A more complete bathymetry coverage, including the axial valley walls, would be necessary to fully address this question.

[34] Another point arguing for the potential role of serpentinization in the distribution of the deformation is a first-order analysis of the distribution of earthquake epicenters along the eastern SWIR. It shows that less earthquakes occurred in the last 30 years east of the Melville transform fault than west of it, except for a cluster near segment 8 at 65°30′E (Figure 1). The record only spans the last 30 years, so that gaps in the seismicity may be explained by the accumulation of stress along

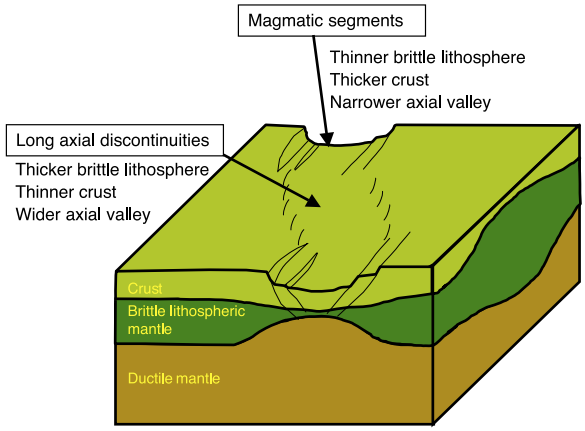

Figure 17. Sketch illustrating the role of brittle lithosphere thickness in the axial morphology, valley width, and amagmatic section length. A thicker brittle lithosphere under amagmatic oblique sections is probably responsible for the larger width of their axial valley compared to spreading perpendicular, magmatically robust sections which have a thinner brittle lithosphere. The thick brittle lithosphere also results in longer discontinuities compared to faster spreading systems like the MAR.

faults which have not ruptured in the considered time window. These gaps, however, could also be explained by the absence of large earthquakes in areas of thin crust, where extension affects mostly serpentinized peridotites. Because serpentine has a lower resistance to deformation than basaltic rocks, and partially serpentinized peridotite behaves like pure serpentine [*Escartín et al.*, 1997], extensional strain in these areas could occur by unrecorded small earthquakes and by plastic flow.

6. Conclusions

[35] We have analyzed the tectonics of two sections of the SWIR from side-scan sonar images. The robust magmatic segments have axial valleys and major faults subperpendicular to spreading. The other sections show oblique spreading with various degrees of obliquity, and numerous, oblique, shorter faults. The images reveal the development of a corrugated surface near 59°E interpreted to be an incipient detachment fault. The faults display two main orientations, typical of oblique rifting tectonic settings. One fault population is subperpendicular to spreading, and the other trends N65–75°E. The oblique faults are probably associated to strike-slip component. The faults are often arranged in left-stepping echelons, also accommodating part of the strike-slip deformation in oblique ridge sections.

[36] The large width of magmatically poor, oblique sections of the SWIR, and the difference in tectonic style between the robust and the magma-starved sections, might be accounted for by large variations in the brittle lithosphere thickness.

[37] Two factors likely control the distribution and style of the deformation in our survey area. First, the large thickness of the brittle lithosphere in some sections might favor the development of multiple faults rather than a single large-offset fault. The emplacement of mantle rocks in the axial valley of our surveyed zones may occur by alternating conjugate faults. Second, serpentinization of outcropping peridotites might be significant in the development of faults in thin crust regions and the distribution of deformation in space and time.

Acknowledgments

[38] We thank the members of the FUJI Scientific Team: Ph. Blondel, D. Boulanger, A. Evans, H. Fujimoto, C. German, Sang-Mook Lee, C. Rommevaux-Jestin, Y. Osada, P. Patriat, G. Pouliquen, R. Searle, K. Tamaki, C. Tamura, T. Yamada, and T. Yama-ashi. We are grateful to Captain Patrick Regnier, the officers and crew of the N/O *Marion Dufresne*, and Yvon Balu, Bernard Olivier, Christopher Flewellen, Robert Wallace, and Duncan Matthews for support in data acquisition. Thanks to Eric Humler and Catherine Mével for the EDUL cruise results. We are indebted to Lindsay Parson for his help in sonar image interpretation and helpful discussions and to Chiori Tamura, Alan Evans, and Tim LeBas for help in data processing. Figures were created using GMT software [*Wessel and Smith*, 1991]. Ship time and TOBI operations were cofunded by Japan, France, and the European Community. Thorough reviews by Catherine Mével and two anonymous reviewers led to considerable improvement of this paper.

References

Allemand, P., and J. P. Brun (1991), Width of continental rifts and rheological layering of the lithosphere, *Tectonophysics*, *188*, 63–69.

Allerton, S., B. J. Murton, R. C. Searle, and M. Jones (1995), Extensional faulting and segmentation of the Mid-Atlantic Ridge north of the Kane Fracture Zone, *Mar. Geophys. Res.*, *17*, 37–61.

Audin, L. (1999), Pénétration de la dorsale d'Aden dans la dépression Afar entre 20 et 4 Ma, doctoral thesis, 318 pp., Univ. Denis Diderot (Paris VII), Paris.

Briais, A., and M. Rabinowicz (2002), Temporal variations of the segmentation of slow to intermediate spreading mid-ocean ridges: 1. Synoptic observations based on satellite altimetry data, *J. Geophys. Res.*, *107*(B5), 2098, doi:10.1029/2001JB000533.

Briais, A., H. Sloan, L. M. Parson, and B. J. Murton (2000), Accretionary processes in the axial valley of the Mid-Atlantic Ridge 27°N–30°N from TOBI side-scan sonar images, *Mar. Geophys. Res.*, *21*(1), 87–119.

Canales, J. P., B. E. Tucholke, and J. A. Collins (2004), Seismic reflection imaging of an oceanic detachment fault: Atlantis megamullion (Mid-Atlantic Ridge 30°10′N), *Earth Planet. Sci. Lett.*, *222*(2), 543–560.

Cann, J. R., D. K. Blackman, D. K. Smith, E. McAllister, B. Janssen, S. Mello, E. Avgerinos, A. R. Pascoe, and J. Escartín (1997), Corrugated slip-surfaces formed at ridge-transform intersections on the Mid-Atlantic Ridge, *Nature*, *385*, 329–332.

Cannat, M., C. Rommevaux-Jestin, D. Sauter, C. Deplus, and V. Mendel (1999), Formation of the axial relief at the very slow spreading Southwest Indian Ridge (49° to 69°E), *J. Geophys. Res.*, *104*(B10), 22,825–22,843.

Cannat, M., C. Rommevaux-Jestin, and H. Fujimoto (2003), Melt supply variations to a magma-poor ultra-slow spreading ridge (Southwest Indian Ridge 61° to 69°E), *Geochem. Geophys. Geosyst.*, *4*(8), 9104, doi:10.1029/2002GC000480.

Cannat, M., D. Sauter, V. Mendel, K. Okino, E. Humler, and C. Mével (2004), Spreading geometry and melt supply at the ultraslow-spreading Southwest Indian Ridge, *Eos Trans. AGU*, *85*(47), Fall Meet. Suppl., Abstract T11G-03.

Clifton, A. E., R. W. Schlisch, M. O. Withjack, and R. V. Ackermann (2000), Influence of rift obliquity on fault-population systematics: Results of experimental clay models, *J. Struct. Geol.*, *22*, 1491–1509.

Dauteuil, O., and J. P. Brun (1996), Deformation partitioning in a slow-spreading ridge undergoing oblique extension (Mohns ridge, Norwegian Sea), *Tectonics*, *15*, 870–884.

Dauteuil, O., J.-P. Brun, F. Avedik, and L. Geli (1990), Caractéristiques structurales du rifting oblique dans la ride de Mohns (Mer de Norvège), *C. R. Acad. Sci., Ser. II*, *311*, 357–363.

Dauteuil, O., P. Huchon, F. Quemeneur, and T. Souriot (2001), Propagation of an oblique spreading center: The western Gulf of Aden, *Tectonophysics*, *332*, 423–442.

DeMets, C., R. G. Gordon, D. F. Argus, and S. Stein (1990), Current plate motions, *Geophys. J. Int.*, *101*, 425–478.

Dick, H. J. B., J. Lin, and H. Schouten (2003), An ultraslow-spreading class of ocean ridge, *Nature*, *426*, 405–412.

Escartín, J., G. Hirth, and B. Evans (1997), Effects of serpentinization on the lithospheric strength and the style of normal faulting at slow-spreading ridges, *Earth Planet. Sci. Lett.*, *151*, 181–189.

Escartín, J., P. A. Cowie, R. C. Searle, S. Allerton, N. C. Mitchell, C. J. MacLeod, and A. P. Slootweg (1999), Quantifying tectonic strain and magmatic accretion at a slow spreading ridge segment, Mid-Atlantic Ridge, 29°N, *J. Geophys. Res.*, *104*(B5), 10,421–10,437.

Fisher, R. L., and A. M. Goodwillie (1997), The physiography of the Southwest Indian Ridge, *Mar. Geophys. Res.*, *19*, 451–455.

Flewellen, C., N. W. Millard, and I. Rouse (1993), TOBI, a vehicle for deep ocean survey, *Electron. Comm. Eng. J.*, *5*(2), 85–94.

Fujimoto, H., et al. (1999), First submersible investigations of mid-ocean ridges in the Indian Ocean, *InterRidge News*, *8*(1), 22–24.

Grindlay, N. R., and P. J. Fox (1993), Lithospheric stresses associated with non-transform offsets of the Mid-Atlantic Ridge: Implications from a finite-element analysis, *Tectonics*, *12*, 982–1003.

Grindlay, N. R., P. J. Fox, and P. R. Vogt (1992), Morphology and tectonics of the Mid-Atlantic Ridge (25°S–27°30′S) from SeaBeam and magnetic data, *J. Geophys. Res.*, *97*(B5), 6983–7010.

Kuo, B.-Y., and D. W. Forsyth (1988), Gravity anomalies of the ridge-transform system in the South Atlantic between 31° and 34.5°S: Upwelling centers and variations in crustal thickness, *Mar. Geophys. Res.*, *10*, 205–232.

Kurras, G. J., S. Gauger, P. J. Michael, J. Thiede, H. J. B. Dick, T. Hartmann, J. Hatzky, W. Jokat, and C. H. Langmuir (2001), Axial valley morphology of the Gakkel ridge (8°W–8°E): Seabeam and hydrosweep bathymetry from the Arctic Mid-Ocean Ridge Expedition (AMORE 2001), *Eos Trans. AGU*, *82*(47), Fall Meet. Suppl., Abstract T11B-0855.

Lagabrielle, Y., et al. (1998), Ultramafic-mafic plutonic rock suites exposed along the Mid-Atlantic Ridge (10°N–30°N). Symmetrical-asymmetrical distribution and implications for seafloor spreading processes, in *Faulting and Magmatism at Mid-Ocean Ridges*, *Geophys. Monogr. Ser.*, vol. 106, edited by W. R. Buck et al., pp. 153–176, AGU, Washington, D. C.

Lavier, L. L., and W. R. Buck (2002), Half graben versus large-offset low-angle normal fault: Importance of keeping cool during normal faulting, *J. Geophys. Res.*, *107*(B6), 2122, doi:10.1029/2001JB000513.

Lawson, K., R. C. Searle, J. A. Pearce, P. Browning, and P. Kempton (1996), Detailed volcanic geology of the MARNOK area, Mid Atlantic Ridge north of Kane transform, in *Tectonic, Magmatic, Hydrothermal and Biological Segmentation of Mid-Ocean Ridges*, edited by C. J. Leod, P. A. Tyler, and C. L. Walker, *Geol. Soc. Spec. Publ.*, *118*, 61–102.

LeBas, T. P., and V. Hühnerbach (1998), PRISM: Processing of Remotely-sensed Imagery for Seafloor Mapping: A collection of software for the processing, analysis and enhancement of sidescan sonar imagery, technical report, 76 pp., Southampton Oceanogr. Cent., Southampton, UK.

Lin, J., G. M. Purdy, H. Schouten, J.-C. Sempéré, and C. Zervas (1990), Evidence from gravity data for focused magmatic accretion along the Mid-Atlantic Ridge, *Nature*, *344*, 627–632.

Macdonald, K. C., P. J. Fox, L. J. Perram, M. F. Eisen, R. M. Haymon, S. P. Miller, S. M. Carbotte, M.-H. Cormier, and A. N. Shor (1988), A new view of the mid-ocean ridge from the behaviour of ridge-axis discontinuities, *Nature*, *335*, 217–225.

Manighetti, I. (1993), Dynamique des systèmes extensifs en Afar, Ph.D. thesis, 242 pp., Paris VI, Paris.

Mauduit, T., and O. Dauteuil (1996), Small-scale models of oceanic transform zones, *J. Geophys. Res.*, *101*(B9), 20,195–20,209.

McAllister, E., and J. R. Cann (1996), Initiation and evolution of boundary-wall faults along the Mid-Atlantic Ridge, 25–29° north, in *Tectonic, Magmatic, Hydrothermal and Biological Segmentation of Mid-Ocean Ridges*, edited by C. J. MacLeod et al., *Geol. Soc. Spec. Publ.*, *188*, 29–48.

Mendel, V., D. Sauter, L. Parson, and J.-R. Vanney (1997), Segmentation and morphotectonic variations along a super slow-spreading center: The Southwest Indian Ridge (57°E–70°E), *Mar. Geophys. Res.*, *19*, 505–533.

Mendel, V., D. Sauter, P. Patriat, and M. Munschy (2000), Relationship of the Central Indian Ridge segmentation with the evolution of the Rodrigues Triple Junction for the past 8 Myr, *J. Geophys. Res.*, *105*(B7), 16,563–16,575.

Mendel, V., D. Sauter, C. Rommevaux-Jestin, P. Patriat, F. Lefebvre, and L. M. Parson (2003), Magmato-tectonic cyclicity at the ultra-slow spreading Southwest Indian Ridge: Evidence from variations of axial volcanic ridge morphology

and abyssal hills pattern, *Geochem. Geophys. Geosyst.*, *4*(5), 9102, doi:10.1029/2002GC000417.

Mével, C., and the EDUL Scientific Party (1997), Sampling the South West Indian Ridge: First results of the EDUL cruise (R/V *Marion Dufresne II*, August 1997), *InterRidge News*, *6*(2), 25–26.

Mével, C., K. Tamaki, and the FUJI Scientific Party (1998), Imaging an ultra-slow spreading ridge: First results of the FUJI cruise on the SWIR (R/V *Marion Dufresne*, 7/10–3/11/97), *InterRidge News*, *7*(1), 29–32.

Meyzen, C. H., M. J. Toplis, E. Humler, J. N. Ludden, and C. Mével (2003), A discontinuity in mantle composition beneath the southwest Indian ridge, *Nature*, *421*, 731–733.

Mitchell, N. C., M. A. Tivey, and P. Gente (2000), Seafloor slopes at mid-ocean ridges from submersible observations and implications for interpreting geology from seafloor topography, *Earth Planet. Sci. Lett.*, *183*, 543–555.

Murton, B. J., and L. M. Parson (1993), Segmentation, volcanism and deformation of oblique spreading centers: A quantitative study of the Reykjanes Ridge, *Tectonophysics*, *222*, 237–257.

Okino, K., D. Curewitz, M. Asada, K. Tamaki, P. Vogt, and K. Crane (2002), Preliminary analysis of the Knipovich Ridge segmentation: Influence of focused magmatism and ridge obliquity on an ultraslow spreading system, *Earth Planet. Sci. Lett.*, *202*, 275–288.

Parson, L. M., et al. (1993), En echelon axial volcanic ridges at the Reykjanes Ridge: A life cycle of volcanism and tectonics, *Earth Planet. Sci. Lett.*, *117*, 73–87.

Parson, L., D. Sauter, V. Mendel, P. Patriat, and R. Searle (1997), Evolution of the axial geometry of the Southwest Indian Ocean Ridge between the Melville Fracture zone and the Indian Ocean Triple Junction–Implications for segmentation on very slow-spreading ridges, *Mar. Geophys. Res.*, *19*, 535–552.

Parson, L. M., E. Gracia, D. Coller, C. German, and D. Needhan (2000), Second order segmentation—The relationship between volcanism and tectonism at the MAR, 38°N–35°40′N, *Earth Planet. Sci. Lett.*, *178*, 231–251.

Patriat, P., D. Sauter, M. Munschy, and L. Parson (1997), A survey of the southwest Indian Ridge axis between Atlantis II fracture zone and the Indian Ocean Triple Junction: Regional setting and large scale segmentation, *Mar. Geophys. Res.*, *19*, 457–480.

Rabinowicz, M., and A. Briais (2002), Temporal variations of the segmentation of slow to intermediate spreading mid-ocean ridges: 2. A three-dimensional model in terms of lithosphere accretion and convection within the partially molten mantle beneath the ridge axis, *J. Geophys. Res.*, *107*(B6), 2110, doi:10.1029/2001JB000343.

Rommevaux-Jestin, C., C. Deplus, and P. Patriat (1997), Mantle Bouguer anomaly along an ultra slow-spreading ridge: Implications for accretionary processes and comparison with results from central Mid-Atlantic Ridge, *Mar. Geophys. Res.*, *19*, 481–503.

Sandwell, D. T., and W. H. F. Smith (1997), Marine gravity anomaly from GEOSAT and ERS-1 satellite altimetry, *J. Geophys. Res.*, *102*, 10,039–10,054.

Sauter, D., P. Patriat, C. Rommevaux-Jestin, M. Cannat, A. Briais, and Gallieni Shipboard Scientific Party (2001), The Southwest Indian Ridge between 49°15′E and 57°E: Focused accretion and magma redistribution, *Earth Planet. Sci. Lett.*, *192*, 303–317.

Sauter, D., L. Parson, V. Mendel, C. Rommevaux-Jestin, O. Gomez, A. Briais, C. Mével, K. Tamaki, and the FUJI Scientific Team (2002), TOBI sidescan sonar imagery of the very slow-spreading Southwest Indian Ridge: Evidence for along-axis magma distribution, *Earth Planet. Sci. Lett.*, *199*, 81–95.

Sauter, D., V. Mendel, C. Rommevaux-Jestin, L. M. Parson, H. Fujimoto, C. Mével, M. Cannat, and K. Tamaki (2004), Focused magmatism versus amagmatic spreading along the ultra-slow spreading Southwest Indian Ridge: Evidence from TOBI side scan sonar imagery, *Geochem. Geophys. Geosyst.*, *5*, Q10K09, doi:10.1029/2004GC000738.

Searle, R. C., M. Cannat, K. Fujioka, C. Mével, H. Fujimoto, A. Bralee, and L. Parson (2003), FUJI Dome: A large detachment fault near 64°E on the very slow-spreading southwest Indian Ridge, *Geochem. Geophys. Geosyst.*, *4*(8), 9105, doi:10.1029/2003GC000519.

Sempéré, J.-C., J. Lin, H. S. Brown, H. Schouten, and G. M. Purdy (1993), Segmentation and morphotectonic variations along a slow-spreading center: The Mid-Atlantic ridge (24°00′N–30°40′N), *Mar. Geophys. Res.*, *15*, 153–200.

Seyler, M., M. Cannat, and C. Mével (2003), Evidence for major-element heterogeneity in the mantle source of abyssal peridotites from the Southwest Indian Ridge (52° to 68°E), *Geochem. Geophys. Geosyst.*, *4*(2), 9101, doi:10.1029/2002GC000305.

Sylvester, A. G. (1988), Strike-slip faults, *Geol. Soc. Am. Bull.*, *100*, 1666–1703.

Tamaki, K., C. Mével, and the FUJI Scientific Party (1998), Spreading tectonics of the eastern part of the Southwestern Indian Ridge: A synthesis of FUJI expedition, *Eos Trans. AGU*, Fall Meeting, *79*(45), F892.

Tron, V., and J.-P. Brun (1991), Experiments on oblique rifting in brittle-ductile systems*Tectonophysics*, *188*, 71–84.

Tucholke, B. E., J. Lin, M. C. Kleinrock, M. A. Tivey, T. B. Reed, J. Goff, and G. E. Jaroslow (1997), Segmentation and crustal structure of the western Mid-Atlantic Ridge flank, *J. Geophys. Res.*, *102*, 10,203–10,223.

Tucholke, B. E., J. Lin, and M. C. Kleinrock (1998), Megamullions and mullion structure defining oceanic metamorphic core complexes on the Mid-Atlantic Ridge, *J. Geophys. Res.*, *103*(B5), 9857–9866.

Tuckwell, G. W., J. M. Bull, and D. J. Sanderson (1998), Numerical models of faulting at oblique spreading centers, *J. Geophys. Res.*, *103*, 15,473–15,482.

Wessel, P., and W. H. F. Smith (1991), Free software helps map and display data, *Eos Trans. AGU*, *72*(41), 441.

Withjack, M. O., and W. R. Jamison (1986), Deformation produced by oblique rifting, *Tectonophysics*, *126*, 99–124.